ADVANCED FUNCTIONAL MATERIALS
www.afm-journal.de

Defect-Healing in Perovskite Photovoltaics Driving Long-Term Reliability and Performance

Xiaochun Zhang, Qing Cao, Luyao Wang, Tiankai Zhang, Kaiyu X. Fu, Zhe Li, Antonio Abate, Meng Li,* and Guixiang Li**

Perovskite solar cells (PSCs) have achieved remarkable power conversion efficiencies exceeding 27%, yet their commercial deployment remains hindered by intrinsic instabilities and vulnerability to environmental stressors. Self-healing strategies have emerged as a promising route to address these limitations by enabling in-operando repair of defects arising from light, moisture, heat, and mechanical stress. This review outlines degradation pathways, distinguishing between reversible and irreversible processes, and the fundamental mechanisms that enable defect healing. Three primary strategies systematically discussed are: i) composition engineering to tune defect dynamics, ii) incorporation of robust polymer/hybrid networks to suppress mechanical and environmental degradation, and iii) dynamic bonding systems that enable reversible structural healing. Representative studies are analyzed in terms of activation conditions, healing mechanisms, and stability improvements under bending fatigue, thermal cycling, and long-term light exposure. Beyond mechanistic insights, this review uniquely bridges fundamental insights with scalable application prospects, including roll-to-roll manufacturing, flexible electronics, and building-integrated photovoltaics. The compatibility of self-healing frameworks with industrial encapsulation and packaging, offering a pathway from lab-scale demonstrations to industrial-scale deployment is also examined. By integrating multi-triggered healing chemistries with large-area manufacturing, these strategies pave the way toward durable, high-performance, and commercially viable PSC technologies for real-world energy applications.

1. Introduction

As an emerging photovoltaic (PV) technology, perovskite solar cells (PSCs) have sparked a research boom in both academia and industry. Their excellent optoelectronic properties, continuously improving efficiency, low raw material costs, and solution-based processing techniques demonstrate enormous potential to reshape the photovoltaic market, sparking optimism and excitement about the future of solar energy.[1–3] To date, the efficiency of single-junction perovskite solar cells has exceeded 27%.[4,5] Despite these remarkable leaps in efficiency, the long-term operational stability of devices under complex real-world conditions remains the primary bottleneck hindering their large-scale commercialization. This underscores the urgent need for research and development in this field.[6–8] Key stability challenges encompass intrinsic material instabilities (e.g., ion migration, phase decomposition),[9–12] environmental factors (e.g., humidity, heat),[13–15] degradation from large-area fabrication,[16–18] and inherently short operational lifetimes of devices.[19–21]

X. Zhang, T. Zhang, G. Li
School of Materials Science and Engineering
Southeast University
Nanjing, Jiangsu 211189, China
E-mail: guixiang.li@seu.edu.cn

Q. Cao, K. X. Fu
Department of Chemistry and Biochemistry
University of Notre Dame
Notre Dame, IN 46556, USA
E-mail: qcao2@nd.edu

L. Wang
State Key Lab for Physical Chemistry of Solid Surfaces
Department of Chemistry
College of Chemistry and Chemical Engineering
Pen-Tung Sah Institute of Micro-Nano Science and Technology
Xiamen University
Xiamen 361005, China

Z. Li
School of Engineering and Materials Science (SEMS)
Queen Mary University of London
London E1 4NS, UK

A. Abate
Helmholtz-Zentrum Berlin für Materialien und Energie GmbH
Hahn-Meitner-Platz 1, 14109 Berlin, Germany

A. Abate
Department of Chemical
Materials and Production Engineering
University of Naples Federico II
Piazzale Tecchio, 80, Naples 80125, Italy

A. Abate
Department of Chemistry
Bielefeld University
Universitätsstraße 25, 33615 Bielefeld, Germany

The ORCID identification number(s) for the author(s) of this article can be found under https://doi.org/10.1002/adfm.202523417

DOI: 10.1002/adfm.202523417

In recent years, considerable efforts have been devoted to improving the stability of perovskite materials through strategies such as passivation engineering,[22–24] additive engineering,[25,26] and full-device encapsulation.[27,28] Once the initial protective measures lose efficacy, devices undergo irreversible performance decline, ultimately limiting their operational lifetimes. However, the potential of in-operando defect repair through self-healing strategies holds significant promise for overcoming this long-standing stability bottleneck, instilling hope and optimism in the future of perovskite photovoltaics and other optoelectronic applications.[29]

Inspired by the self-healing capabilities found in nature, researchers have developed self-healing materials and advanced their translation into product applications.[30–32] The mechanisms of action for such materials involve physical or chemical processes, such as ion migration, defect repair, and structural reorganization within perovskite materials. These processes can occur spontaneously or be triggered by external stimuli.[33–35] Furthermore, common environmental factors that usually accelerate perovskite degradation, including light,[36] moisture/oxygen,[37–39] and temperature,[40,41] can also serve as triggers for self-healing. By introducing these factors into the perovskite film, the very elements that harm stability can be transformed into agents that repair damaged materials in devices, thereby significantly extending their operational lifetime.[42–44] Alternatively, dynamic self-healing can take place under mild conditions (e.g., removal of illumination or heat stress). In this mechanism, spontaneously migrating ions and structural relaxation repair reversible defects induced by photo/electrical stress, restoring optoelectronic properties and enhancing device stability.[45–47]

2. Degradation Mechanisms of Perovskites

2.1. Light-Induced Reactions

Light exposure is a key environmental stressor that triggers complex physicochemical changes in perovskite materials, leading to structural decay, performance loss, and eventual device failure.[48,49] Understanding the intrinsic mechanisms behind this light-induced degradation is essential for developing effective strategies to improve stability and extend device lifespan. This chapter systematically explores the primary degradation pathways responsible for the photochemical instability of halide perovskites, providing a foundation for designing optically stable and self-healing perovskite systems.

For perovskite devices, the simultaneous presence of light and oxygen drastically accelerates material decomposition and severely compromises stability. However, illumination alone remains sufficient to induce perovskite degradation.[15,50] Furthermore, ultraviolet (UV) radiation exerts a particularly pronounced destabilizing influence on these materials. Under UV exposure, $MAPbI_3$ perovskite undergoes either reversible or irreversible degradation.[51,52] The resultant decomposition product, lead iodide (PbI_2), may further degrade through chain reactions, as illustrated in Equations (1)–(3). Critically, the decomposition of $MAPbI_3$ not only directly impairs device performance but also facilitates the formation of metallic lead (Pb^0). This elemental Pb^0 significantly enhances non-radiative recombination within the device, thereby impeding charge carrier transport and exacerbating efficiency losses.[53,54]

$$CH_3NH_3PbI_3 \rightarrow NH_3 + CH_3I + PbI_2 \quad (1)$$

$$CH_3NH_3PbI_3 \leftrightarrow CH_3NH_2 + HI + PbI_2 \quad (2)$$

$$PbI_2 \leftrightarrow Pb^0 + I_2 \quad (3)$$

As described in Equation (1), $MAPbI_3$ undergoes irreversible degradation, producing volatile gases methyl iodide (CH_3I), ammonia (NH_3), and lead iodide (PbI_2). Equation (2) depicts the reversible decomposition pathway of $MAPbI_3$, yielding methylammonium (CH_3NH_3), hydrogen iodide (HI), and PbI_2. Initially, the presence of PbI_2 was considered beneficial, acting as an optical filter that mitigates further degradation.[55,56] Furthermore, an appropriate amount of PbI_2 can passivate defects at perovskite grain boundaries and interfaces.[57] Paradoxically, as PbI_2 accumulates, the degradation rate accelerates, leading to the reaction shown in Equation (3), where PbI_2 decomposes into metallic lead (Pb^0) and elemental iodine (I_2). This process ultimately drives the progressive structural collapse of the perovskite material.

Current understanding indicates that the reversible pathway primarily dominates the photodegradation of $MAPbI_3$. Yan et al. proposed that at room temperature, CH_3NH_3 and HI are the main decomposition products (**Figure 1**a,b). Under light excitation, photogenerated carriers facilitate the deprotonation of $CH_3NH_3^+$, leading to the formation of methylamine and mobile protons. These mobile protons, in turn, participate in further secondary reactions, indirectly accelerating the additional decomposition of MA^+. The mobile protons interact with surface iodide ions (I^-), producing volatile HI and creating iodide vacancies (V_I). Significantly, the reversible nature of these light-induced reactions provides a mechanistic foundation for the observed self-healing of perovskite device efficiency.[52] Similarly, Qi et al. demonstrated the thermodynamically reversible decomposition of hybrid lead halide perovskites under mild visible-light irradiation at ambient temperatures. As schematized in Figure 1c, this process establishes a perpetual cycle of dissociation and reformation wherein gaseous decomposition byproducts maintain chemical equilibrium.[51] Experimental validation was achieved through photodecomposition assays of PbI_2 within a custom-designed reaction chamber (Figure 1d,e). In situ spectroscopic monitoring confirmed the regeneration of perovskite phases, substantiating the equilibrium-driven healing mechanism.

To assess the PSCs' photostability, Dalal et al. exposed devices to full-spectrum sunlight for 100 h (Figure 1f). During this period, the open-circuit voltage (*Voc*) increased until reaching

M. Li
Key Lab for Special Functional Materials of Ministry of Education
National and Local Joint Engineering Research Center for High-Efficiency Display and Lighting Technology
School of Nanoscience and Materials Engineering
Collaborative Innovation Center of Nano Functional Materials and Applications
Henan University
Kaifeng 475004, China
E-mail: mengli@henu.edu.cn

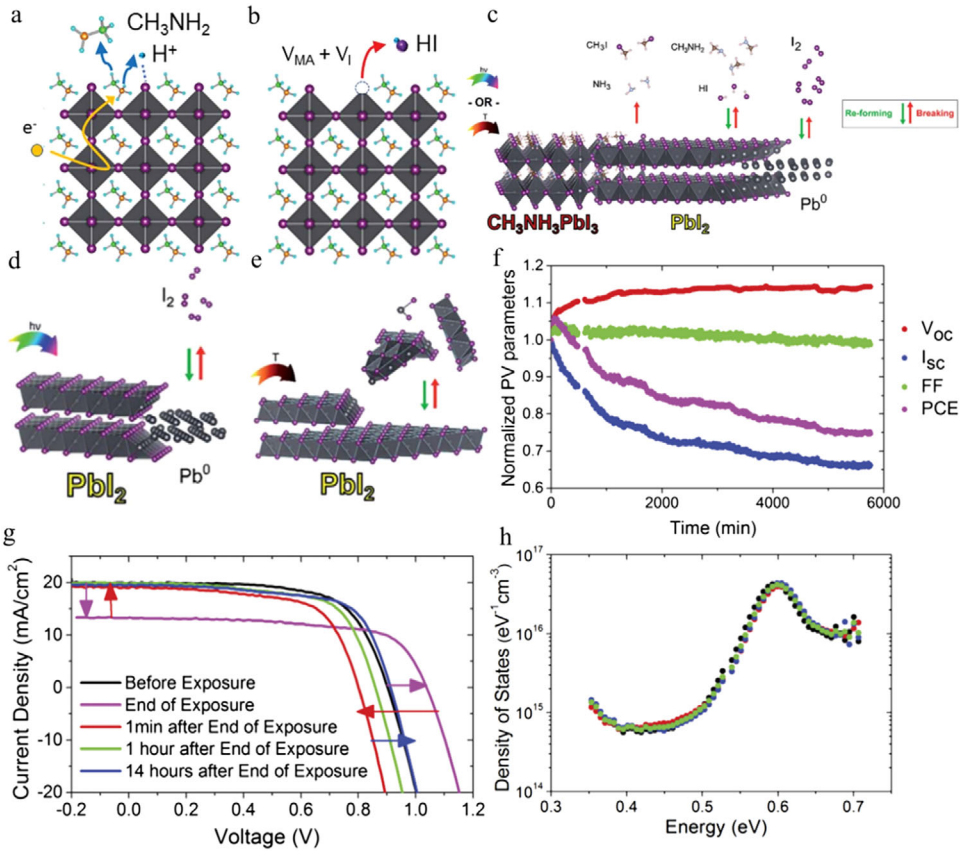

Figure 1. a) Deprotonation and release of MA^+ gas.[52] b) formation of HI gas and VI.[52] Copyright 2018, Royal Society of Chemistry. c) $MAPbI_3$ photodecomposition and thermal degradation processes.[51] d) PbI_2 decomposition process driven by visible light (<530 nm) above the PbI_2 band gap at 40 to 60 °C.[51] e) emperatureassisted PbI_2 evaporation at 70 °C in the dark.[51] Copyright 2018, Juarez-Perez et al. f) Degradation in device performance versus time.[58] g) The recovery of device performance at various times after exposure is stopped and the device is kept in dark at 25 °C.[58] h) Defect density measured using the capacitance-frequency method before and after exposure.[58] (black-before exposure; red-1 min after end of exposure; green-1 h after end of exposure; blue-14 h after end of exposure).Copyright 2016, Joshi et al.[58] This article is distributed under a Creative Commons Attribution (CC BY) license.

saturation, while the short-circuit current density (*Jsc*) exhibited continuous degradation. Subsequently, the devices underwent thermal annealing in the dark. Figure 1g illustrates the evolution of the *J–V* curves after dark annealing: *Jsc* rapidly recovered to its initial value. *Voc* initially dropped below its original level but gradually recovered thereafter. After 14 h of dark storage, the *J–V* characteristics exhibited nearly complete recovery to their pre-degradation state. Their findings (Figure 1h) demonstrate that the electronic density of states (DOS) remained unchanged before and after degradation. This invariance provides direct evidence for the thermally reversible nature of light-induced degradation in these perovskite materials.[58] Similarly, research by Nie et al. examined the evolution of two specific points (A and B, where A-red circles, J = 0, V = *Voc*, B-blue circles, J = *Jsc*, *Voc* = 0) on the *J–V* curves under illumination (**Figure 2a**).[13] Point A exhibited a substantial decrease in power conversion efficiency (PCE), approaching 40%, while the degradation rate at Point B was significantly retarded. Following storage in the dark, the device parameters gradually recovered to their initial values. To explain this phenomenon, they proposed a dynamic degradation model (Figure 2b): under constant 1-sun illumination, the population of photoactivated metastable trap states (red dashed line) continuously increases. These states accumulate over timescales ranging from minutes to hours, leading to the formation of charged regions within the bulk film. Consequently, this charge redistribution drives the observed photocurrent degradation. When the device is placed in darkness, the majority of these photoactivated traps dissipate. Upon subsequent re-illumination, the photocurrent (and consequently the PCE) self-heals, recovering to ≈100% of its initial steady-state value (self-healing mechanism).

2.2. Thermal Stress

A critically important yet inadequately addressed challenge for perovskite devices lies in the inherent thermal instability of the perovskite material itself. According to the international standard IEC 61646, the thermal stability testing for perovskites mandates that devices must maintain stability at 85 °C—a benchmark temperature representing peak rooftop temperatures encountered on hot summer days.[59] Early thermogravimetric analysis (TGA)

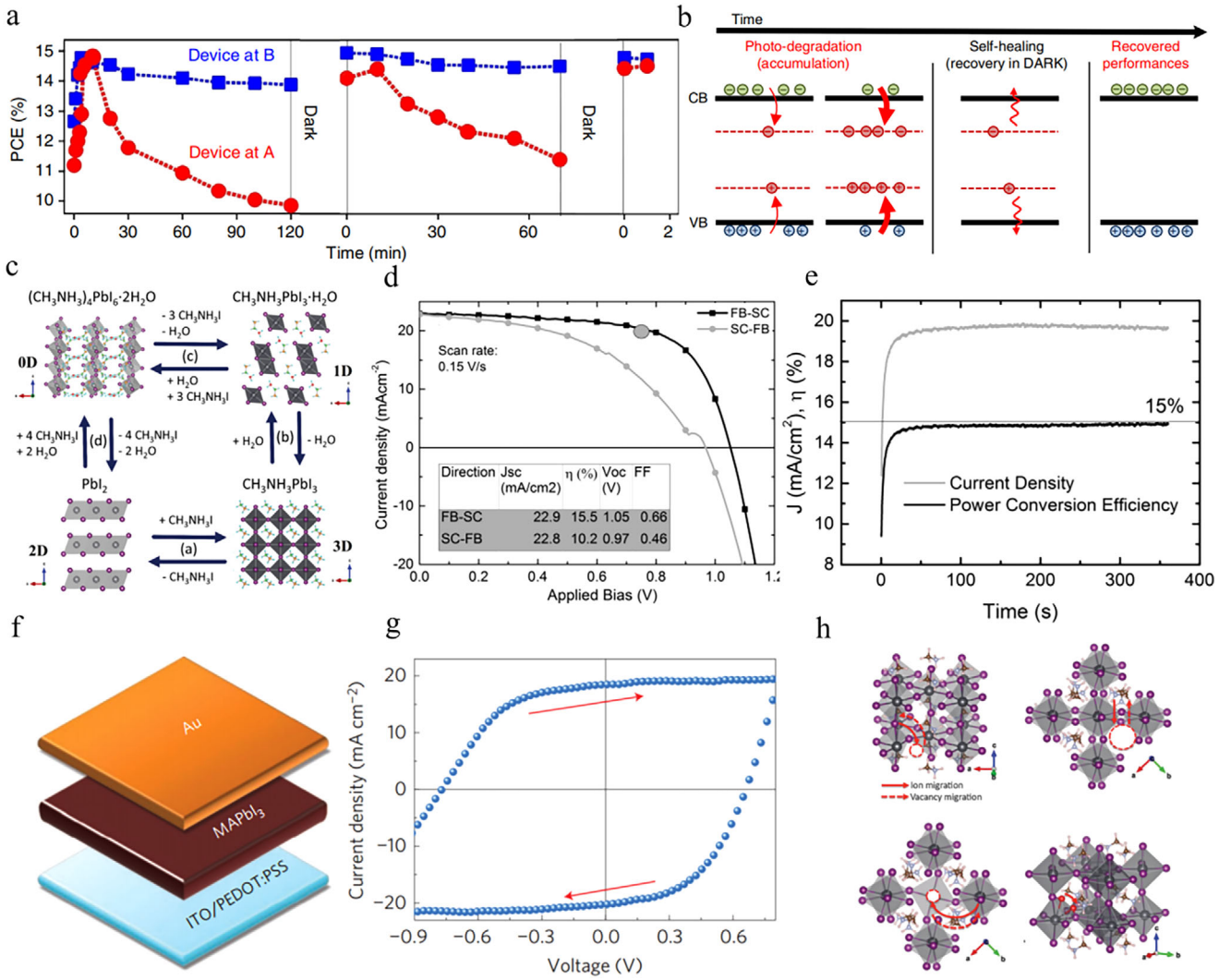

Figure 2. a) Time evolution of device performance and figures of merit under constant 1-sun illumination and after resting the device in the dark.[13] b) Schematics of the proposed photocurrent degradation and self-healing mechanism based on perovskite layer band structure evolution, sketching the valence (VB) and conduction (CB) bands for three situations.[13] Copyright 2016, Wanyi Nie et al. c) Schematic diagram of the phase equilibria in the PbI_2 - CH_3NH_3I H_2O system.[64] Copyright 2016, WILEY-VCH Verlag GmbH & Co. KGaA, Weinheim. d) Forward bias to short circuit (FB-SC) and short circuit to forward bias (SC-FB) current–voltage curves measured under AM 1.5G simulated sunlight for an MSSC.[71] e) Photocurrent density and power conversion efficiency as a function of time for the same cell held close to 0.75 V forward bias.[71] Copyright 2014, American Chemical Society. f) Schematic of the vertical structure device.[72] g) Photocurrent hysteresis curves of the devices under continuous current sweeping at a rate of 0.14 V s^{-1} between −2.5 V and 2.5 V.[72] Copyright 2014, Springer Nature Limited. h) Diffusion paths for the V_i, V_{MA}, V_{Pb}, and I_i defects.[73] Copyright 2015, Royal Society of Chemistry.

studies revealed that $MAPbI_3$ decomposes via two distinct pathways under thermal stress.[60,61]

$$CH_3NH_3PbI_3 \xrightarrow{\Delta} NH_3 + CH_3I + PbI_2 \quad (4)$$

$$CH_3NH_3PbI_3 \xleftrightarrow{\Delta} CH_3NH_2 + HI + PbI_2 \quad (5)$$

Equation (4) represents an irreversible reaction. The decomposition of $MAPbI_3$ into NH_3 and CH_3I is thermodynamically unfavorable for reversal, resulting in permanent degradation of the material. $MAPbI_3$ tended to degrade along Equation (5) at low temperatures. Currently, precise decomposition products under thermal stress remain ambiguous, as they are critically dependent on factors such as device encapsulation, substrate choice, and contact materials.

Compared to $MAPbI_3$, $FAPbI_3$ exhibits superior thermal stability, which can be attributed to two main factors related to its distinct cationic properties. First, the MA^+ is a relatively small and polar molecule, which exhibits significant dipole disorder and dynamic disorder within the perovskite lattice. This molecular-level disorder makes the crystal structure more susceptible to distortion and deformation under thermal stress, thereby lowering the energy barrier for phase transitions. In contrast, the FA^+ is larger and possesses higher molecular symmetry. These characteristics allow it to form a more ordered and

rigid crystal lattice, which better resists thermal degradation. Second, the interaction between the organic cation and the inorganic $[PbI_6]_4^-$ framework differs significantly. MA^+ contains only one N—H group that can form a hydrogen bond with the iodide ions (I^-) in the lattice. This single hydrogen bond is relatively weak and more prone to breaking at elevated temperatures. On the other hand, FA^+ features two N—H groups, enabling the formation of a stronger, bidentate hydrogen-bonding network with the inorganic framework. This enhanced interaction more effectively anchors the FA^+ cation within the lattice, increasing the activation energy for ion migration and structural decomposition. Nevertheless, studies indicate that $FAPbI_3$ undergoes spontaneous transition at room temperature from the photoactive cubic phase (α-$FAPbI_3$, black phase) to the non-photoactive hexagonal phase (δ-$FAPbI_3$, yellow phase). This phase instability constitutes a fundamental origin of its thermal instability.[62,63] Following the formation of the δ-phase, irreversible chemical decomposition occurs under sustained thermal stress. When temperatures exceed 95 °C, the primary decomposition product is symtriazine ($C_3H_3N_3$) (Equation 6). Below 95 °C, reversible reactions generate hydrogen cyanide (HCN) and ammonia (NH_3) (Equation 7). As the temperature progressively rises to 360 °C, HCN becomes the predominant decomposition product.

$$3CH(NH_2)_2PbI_3 \xrightarrow{\Delta} (HCN)_3 + 3NH_3 + 3PbI_2 + 3HI \quad (6)$$

$$CH(NH_2)_2PbI_3 \xrightarrow{\Delta} HCN + NH_3 + PbI_2 + HI \quad (7)$$

2.3. Moisture-Induced Degradation

Exposure to moisture triggers degradation in perovskite materials, significantly compromising their stability. This process involves intricate reaction pathways. Elucidating the underlying degradation mechanisms is crucial for formulating effective self-healing strategies.

As illustrated in Figure 2c, $MAPbI_3$ undergoes sequential hydration upon water exposure (Equation (8)).[64,65] Initial contact forms a 1D hydrated perovskite phase ($CH_3NH_3PbI_3{\cdot}H_2O$). Prolonged water exposure accelerates degradation, reducing the 1 D hydrate to a 0 D hydrated phase ($(CH_3NH_3)_4PbI_6{\cdot}2H_2O$) (Equation 9).[66,67] This hydration process is fully reversible under dry conditions. However, the transformation to the 0 D phase generates PbI_2 as a byproduct through $CH_3NH_3^+$ dissociation.[68] This byproduct formation triggers redistribution of organic and inorganic components, causing compositional inhomogeneity, altered grain volume, and modified film morphology—collectively degrading device optoelectronic performance. Notably, excess ions ($CH_3NH_3^+$ and I^-) in the dehydrated 0 D phase can migrate to adjacent PbI_2-rich domains, ultimately reforming $CH_3NH_3PbI_3$.[69] The complete reaction pathway is shown in the equations below (Equation 10).

$$CH_3NH_3PbI_3 + H_2O \leftrightarrow CH_3NH_3PbI_3 \cdot H_2O \quad (8)$$

$$(4-n)CH_3NH_3PbI_3 + nCH_3NH_3PbI_3 \cdot H_2O + (2-n)H_2O \leftrightarrow (CH_3NH_3)_4PbI_6 \cdot 2H_2O + 3PbI_2 \quad (9)$$

$$(CH_3NH_3)_4PbI_6 \cdot 2H_2O \leftrightarrow PbI_2 + 4CH_3NH_3I + 2H_2O \quad (10)$$

Mitigating moisture infiltration is paramount for enhancing PSCs stability. Within hydrated perovskite crystals, hydrogen bonding between H_2O and organic cations (e.g., $CH_3NH_3^+$) progressively weakens the coordination bonds anchoring these cations to the $[PbI_6]^{4-}$ octahedra. This bond destabilization accelerates deprotonation kinetics of organic moieties while heightening material susceptibility to external stressors—notably thermal excitation and electric fields.[70] Concurrently, water-mediated proton transfer to iodide species generates volatile hydroiodic acid (HI), inducing irreversible mass loss.[70] Crucially, the dual mechanisms of lattice softening and acid corrosion necessitate implementing robust moisture barriers as a fundamental stabilization strategy for operational PSCs.

2.4. Degradation Pathways

As ionic crystals, perovskites face a fundamental stability limitation that device engineering cannot fully resolve, leading to short operational lifetimes. The central issue is ion migration—involving halides, organic/metal cations, and additives—which is triggered by electric fields, light, or heat. This migration causes ion loss, lattice collapse, and changes in film structure, ultimately resulting in material decomposition. Key failure mechanisms include phase segregation, electrode corrosion, interface degradation, and current–voltage hysteresis, all of which accelerate device failure.[74]

Ion migration in metal halide perovskites has been a subject of investigation for decades. As early as 1983, Mizu et al. first reported ion migration phenomena in organometal halide perovskites, proposing that ionic conductivity originated from halogen vacancy (Br, I) migration.[75] However, their study was conducted at 200 °C, far exceeding typical solar cell operating temperatures. Renewed interest in ion migration emerged in 2014, McGehee and Snaith team reported hysteresis in perovskite solar cells with TiO_2 as electron transport layer (Figure 2d,e), where *J*–*V* curves obtained through repeated measurements failed to overlap when voltage scan direction or speed was altered.[71,76,77] They observed that hysteresis in PSCs correlated with scan direction, measurement delay time, and pre-measurement light/voltage bias conditions. Consequently, they suggested that photoinduced ion migration might significantly contribute to device hysteresis. In the same year, Huang et al provided the first conclusive evidence of substantial ion migration in perovskites at room temperature.[72] Their study discovered fully reversible photovoltaic effects in ITO/PEDOT:PSS/$MAPbI_3$/Au structures (Figure 2f,g), characterized by completely inverted photocurrent directions. Based on this, they fabricated lateral $MAPbI_3$-based devices and, through in situ microscopic observation, documented electric-field-induced alterations in film morphology and light absorption properties. The films near the anode region progressively became transparent due to ion migration. Subsequent Kelvin probe force microscopy (KPFM) measurements confirmed changes in surface potential before and after ion migration, representing the first experimental verification of

significant ion migration in perovskites. Ion migration typically coexists with defect formation, while distinct migration patterns lead to variations in defect types.

Fundamentally, when an ion vacates its lattice site, it generates a vacancy defect (Figure 2h). For instance, under electric fields or illumination, migrating halide ions (I^-, Br^-) create negatively charged vacancies (V_x^-). These vacancies act as non-radiative recombination centers that reduce carrier lifetimes, while simultaneously accumulating charge to form low-energy barriers that accelerate subsequent ion migration.[18,73,77,78] In contrast, metal cation vacancies (V_B^{2+})—primarily formed by migrating Pb^{2+} or Sn^{2+} ions - predominantly occur at surfaces and grain boundaries. These vacancies distort the crystal lattice, create deep-level traps in p-type regions, and significantly increase non-radiative recombination losses.[79,80] The formation of interstitial defects occurs when migrating ions occupy interstitial sites instead of filling vacancies. Migrating halide ions synergistically combine with vacancies to create Frenkel defects (I_x^+), which increase leakage current and degrade device performance. Concurrently, halide accumulation at interfaces induces electrode corrosion (e.g., through AgI formation), elevating contact resistance.[81,82] Under proton irradiation or high electric field stress, metal cations deviate from lattice sites into interstitial positions (I_B^{2+}). This lattice displacement causes crystal expansion, initiates microcrack formation, enhances Auger recombination, and ultimately compromises device luminescence efficiency.[81,83]

2.5. Self-Healing Strategies

Focusing on enhancing the self-healing capability and long-term stability of perovskite optoelectronic devices, this research proceeds from four core strategies: composition engineering, robust additive functionalization, dynamic self-healing mechanisms, and application expansion. By regulating the composition of A-site cations, incorporating polymer additives with dynamic bonds, and designing reversible interaction networks, effective recovery of the structure and optoelectronic properties is achieved, providing crucial technical support for the commercialization of perovskite devices. The following is a summary table of specific strategies and performances (**Table 1**):

2.6. Composition Engineering

The structure of perovskites follows the ABX_3 configuration, where the A-site cation, as a key component in perovskite solar cells, exhibits a decomposition mechanism intrinsically linked to the material's inherent instability. Exploring viable methods to enable self-healing is therefore crucial.

Due to differences between perovskite single crystals and their surfaces, Cahen et al. evaluated the stability of single crystals and surfaces of different A-site cation perovskite materials based on Pb and Br to determine the self-healing capacity of various A-site cations.[94] Fluorescence recovery after photobleaching (FRAP) was used to assess the recovery of $APbBr_3$ surfaces. Two different lasers—1P (single-photon confocal microscopy) and 2P (sub-bandgap two-photon confocal illumination)—were employed to simulate the energy released by the sun within seconds, enabling observation of self-healing on the crystal surface and interior, respectively. In **Figure 3a** and in **Table 2**, we summarize all the information on $APbBr_3$ perovskites after photo-bleaching, provided by the current study. Closed circles represent degradation followed by self-healing processes. Red circles describe Bri-related ones and green circles describe methylamine-related processes. Thicker lines correspond to faster processes. Arrows pointing vertically represent material exchange with the environment. Bulk and surface processes are separated by the dotted line, showing that self-healing dominates in the bulk and material loss dominates at the surface. From the FA perovskite in the figure (left column of Figure 3a), it can be observed that the displacement of FA^+ ions caused by Br_i^+ defects is in an energy-unfavorable state in the bulk phase. The system will attempt to recover to its defect-free form, triggering a spontaneous healing mechanism to achieve complete and rapid self-repair. The surface results show that once damaged, FA becomes more stable than MA (methylamine), and its decomposition products are high-boiling aromatic molecules (triazine/triazine), rather than volatile amine acid pairs. For the bulk phase effects of MA cations, two opposing transient phenomena are observed: the photoluminescence (PL) enhancement is attributed to the passivation effect of methylamine, while the PL quenching arises from the chemical nature of bromine interstitial defects (Br_i^+). Regarding surface processes, methylamine (CH_3NH_2) generated from MA perovskite decomposition undergoes recondensation and eventual re-evaporation. Under non-vacuum conditions, partial re-adsorption of methylamine occurs at the surface, yielding beneficial passivation effects. This mechanism partially explains the documented device performance enhancement following short-term light exposure (light soaking).[95,96] The situation for the $CsPbBr_3$ sample is different (right column in Figure 3a). The formation of Br_3^- defects in the bulk requires low energy input and has little impact on the crystal structure, resulting in slow bulk self-healing of Cs-based perovskites and a recovery rate inferior to that of organic analogs containing A cations. At the surface, $CsPbBr_3$ exhibits stronger structural rearrangement capability, with easier migration of decomposition products (excluding oxides). Although the initial energy required for surface decomposition is lower than that of MA, its impact is less significant compared to FA and MA. This could be attributed to the small amount of volatile substances generated and the fact that most of the material can re-form relatively quickly (due to the relaxation of steric constraints). A comprehensive analysis of data from three perovskites reveals that in the mixed A-cation perovskite $MA_xFA_yCs_{1-x-y}PbBr_3$, Cs contributes to surface stabilization, methylamine released by MA can repair bulk defects, and FA ensures long-term stability. It is hypothesized that under stable illumination conditions, a Cs-enriched surface and an FA-enriched bulk will form, a model that awaits verification. Each A-cation exerts distinct influences; when mixed, their synergistic effects, combined with the configurational entropy increase arising from the disordered distribution of A-cations, can enhance the overall stability and performance of the material.

The impact of A-site cation composition on the self-healing behavior of perovskite nanocrystals has been systematically elucidated through the work of Kuo et al., who investigated $Cs_{1-x}FA_xPbBr_3$ hybrid perovskite nanocrystals (HPNCs) with varying Cs^+/FA^+ ratios.[97] Their study revealed that precise

Table 1. Comparative summary table of self-healing strategies for different materials.

Strategy	Functional bond	Material system	Device morphology	Area	Initial value	Testing conditions	Recovery conditions	Efficiency retention
Acylhydrazone bond-containing waterborne polyurethane (Ab-WPU)[84]	Acylhydrazone bond	$FA_{0.96}Cs_{0.04}PbI_{2.8}Br_{0.12}$	Flexible	0.04 cm^2	21.27%	1000 bending cycles	Heated to 60 °C	Recovering 95%
Natural polymerizable small molecule α-lipoic acid (LA)[85]	Dynamic disulfide bond	$Cs_{0.05}(FA_{0.92}MA_{0.08})_{0.95}Pb(I_{0.92}Br_{0.08})_3$	Flexible	0.04 cm^2	19.03%	3000 bending cycles	Mild heat treatment	Recovering 95%
Crosslinking monomer (TA-NI) with dynamic covalent disulfide, hydrogen bond, and ammonium ion[86]	Dynamic covalent disulfide bond, hydrogen bond	$FA_{0.75}MA_{0.25}PbI_3$	Flexible	1.004 cm^2	21.66%	20000 bending cycles		91% retention
						30% relative humidity for 3000 h		93% retention
Self-welding dynamic diselenide (DiSe)[87]	Dynamic diselenide bond	$Cs_{0.05}MA_{0.05}FA_{0.9}PbI_3$	Flexible	1.043 cm^2	24.85%	15000 bending cycles	–	91.8% retention
Self-healing ion-conductive elastomer (ICE) with imidazolium-based ionic liquid[88]	Ion-conductive elastomer	$FA_{0.83}MA_{0.17}PbI_{2.98}Cl_{0.02}$	Flexible	0.04 cm^2	24.84%	Stored in the glove box for 5000 h		92% retention
						10 000 bending cycles	1 h	Recovering 91%
Heat-triggered dynamic self-healing framework (HDSF)[89]	Disulfide bond	$Cs_{0.05}FA_{0.85}MA_{0.1}PbI_3$	Rigid	0.078 cm^2	26.32%	Dark storage at 85 °C for 1000 h		88.7% retention
						160 thermal cycles at 80 °C		92.6% retention
Vapor-deposited multidentate ligand isolating defect octahedra on perovskite surface[90]	–	$FA_{0.76}MA_{0.24}PbI_3$	Large-area rigid module	785 cm^2	19.6%	101 light-dark cycles at 50 °C	Enhanced daytime stability	97% retention
2-(1-cyclohexenyl) ethylammonium functional cation[91]	–	$FA_{0.75}MA_{0.25}PbI_3$	Large-area rigid module	715.1 cm^2	22.49%;	Aged at 65 °C for 500 h; ambient humidity,	–	90% retention
					22.61%	65 °C, encapsulated device aged for 528 h		94% retention
Methylene diphenyl diisocyanate polyurethane (MDI-PU) polymer[92]	–	$CsPbBr_{2.5}Cl_{0.5}/(4\text{-FPEA})_2PbBr_4$	Flexible	10 mm^2	13.5% EQE	2000 Cycles of repeated bending	–	87.8% retention
						2000 cycles of repeated twisting		80.7% retention
Poly(3,4-ethylenedioxythiophene): ethylene-vinyl acetate copolymer[93]	–	$(FA_{0.8}MA_{0.2})PbI_{2.9}Br_{0.1}$	Flexible	1.01 cm^2	19.87%	7000 Narrow bending cycles	–	85% retention

modulation of the Cs/FA molar ratio (i.e., x-value) significantly optimizes crystal structural stability, ion migration kinetics, and defect state density in nanocrystals. Figure 3b–d presents 2D contour plots of time-resolved photoluminescence (TRPL) for $Cs_{0.7}FA_{0.3}PbBr_3$, $Cs_{0.5}FA_{0.5}PbBr_3$, and $Cs_{0.3}FA_{0.7}PbBr_3$ hybrid perovskite nanocrystals (HPNCs), revealing that HPNC films with higher FA^+ content ($x \geq 0.5$) exhibit significantly longer carrier lifetimes than those with lower FA^+ concentrations ($x \leq 0.3$). Crucially, specific Cs/FA ratios (e.g., $x \approx 0.5$) generate pronounced synergistic effects: Cs^+ enhances lattice rigidity and suppresses phase segregation, while the larger size and dynamic nature of FA^+ facilitate reversible lattice relaxation. The

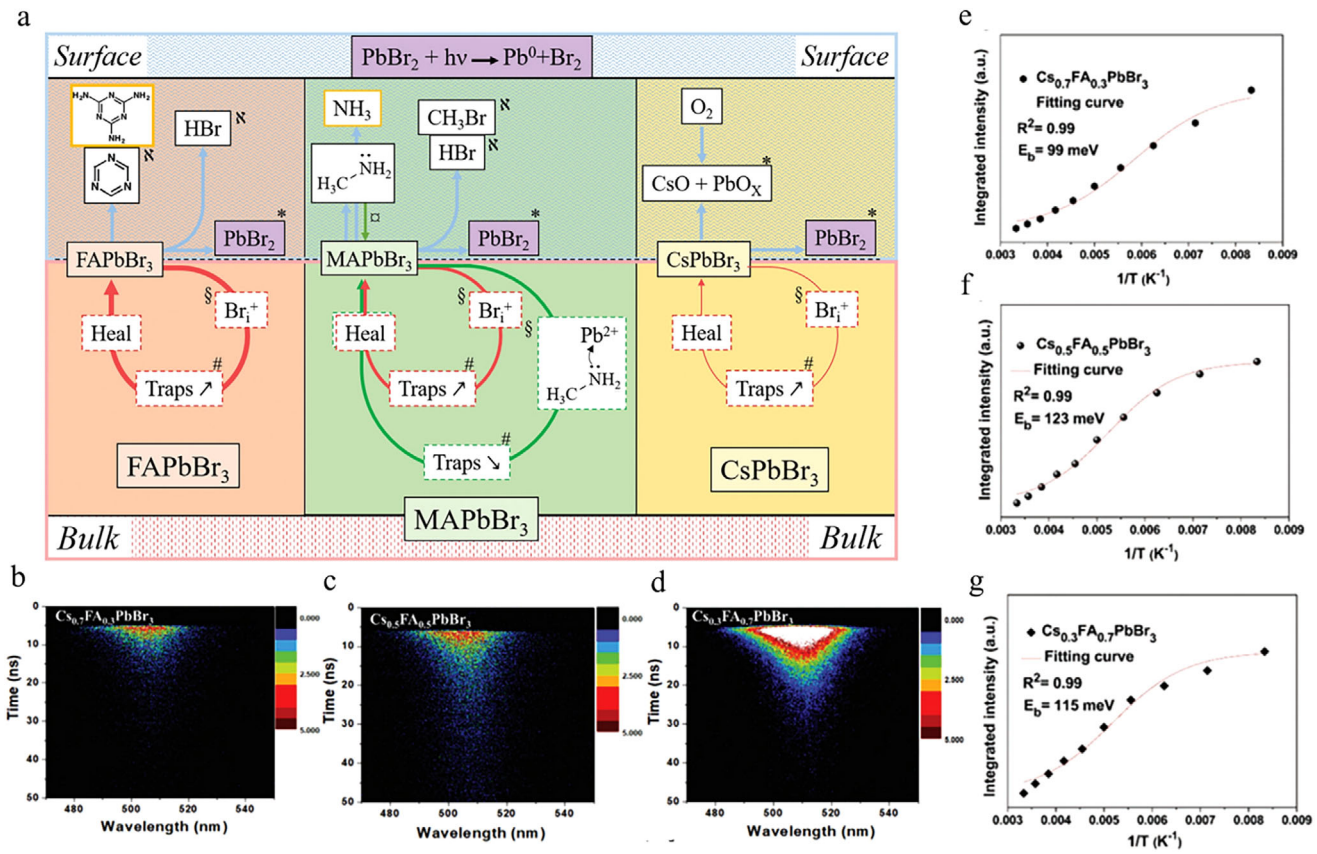

Figure 3. a) Scheme of the chemical processes involved the degradation and healing of $APbBr_3$ perovskites on the surface and in the bulk. The symbols indicate observables, analyzed in the main text, and consistent with the indicated processes: ∫ DFT; # 2P PL Lifetime and intensity; 1P PL Intensity and AFM; * InLens SEM, EDS, and work function increase; ℵ TGA-MS.[94] Copyright 2021, Ceratti et al. b) $Cs_{0.7}FA_{0.3}PbBr_3$, c) $Cs_{0.5}FA_{0.5}PbBr_3$, d) $Cs_{0.3}FA_{0.7}PbBr_3$. Temperature-dependent PL spectra of ST-2-based $Cs_{1-x}FA_xPbBr_3$ HPNCs: e) $Cs_{0.7}FA_{0.3}PbBr_3$, f) $Cs_{0.5}FA_{0.5}PbBr_3$, g) $Cs_{0.3}FA_{0.7}PbBr_3$.[97] Copyright 2023, Wiley-VCH GmbH.

corresponding $Cs_{0.5}FA_{0.5}PbBr_3$ HPNCs exhibits a high Eb value of 123 meV, and larger than other compositions of $Cs_{1-x}FA_xPbBr_3$ HPNCs films (x = 0, 0.3, and 0.7, Figure 3e–g) and previously reported $CsPbBr_3$ (40 meV).[98,99] This confirms that FA^+ doping in $CsPbBr_3$ contributes to an increase in the strength of electron–hole interaction, and improves the carrier transport, resulting in high long-term stability compared with the previous short-living component of $CsPbBr_3$ NCs (≈1 ns) or $FA_{1-x}Cs_xPbBr_3$ systems (≈4.3 ns).[98,100,101] The doping of FA^+ cations and well-surface capping are therefore indispensable components, and represent tremendous advances in increasing the stability of the PeNCs tolerance factor and tuning the exciton recombination kinetics, offering potential merits for application in PeLEDs. This interplay endows the material with exceptional self-healing capabilities-after external stress-induced damage (e.g., electric fields, illumination, or mechanical strain), efficient

Table 2. Summary of the damage and self-healing, and additional phenomena reported in this work for the $APbBr_3$ perovskites.[94]Copyright 2021, Ceratti et al.

Cation	Location	Damage	Healing	Phenomenon	Supported by
MA	Surface	Threshold	Minimal	Halo-MA condensation,Pb/Br increase	AFM-SEM, EDS
	Bulk	Progressive	Fast	Increase/decrease in PL	DFT
FA	Surface	Threshold	Partial	Pb/Br increase	EDS
	Bulk	Progressive	Very fast	Decrease in PL	DFT
Cs	Surface	Threshold	Semi-complete	O-containing product(s),Cs/Pb increase	EDS, XPS
	Bulk	Progressive	Slow	Decrease in PL	DFT

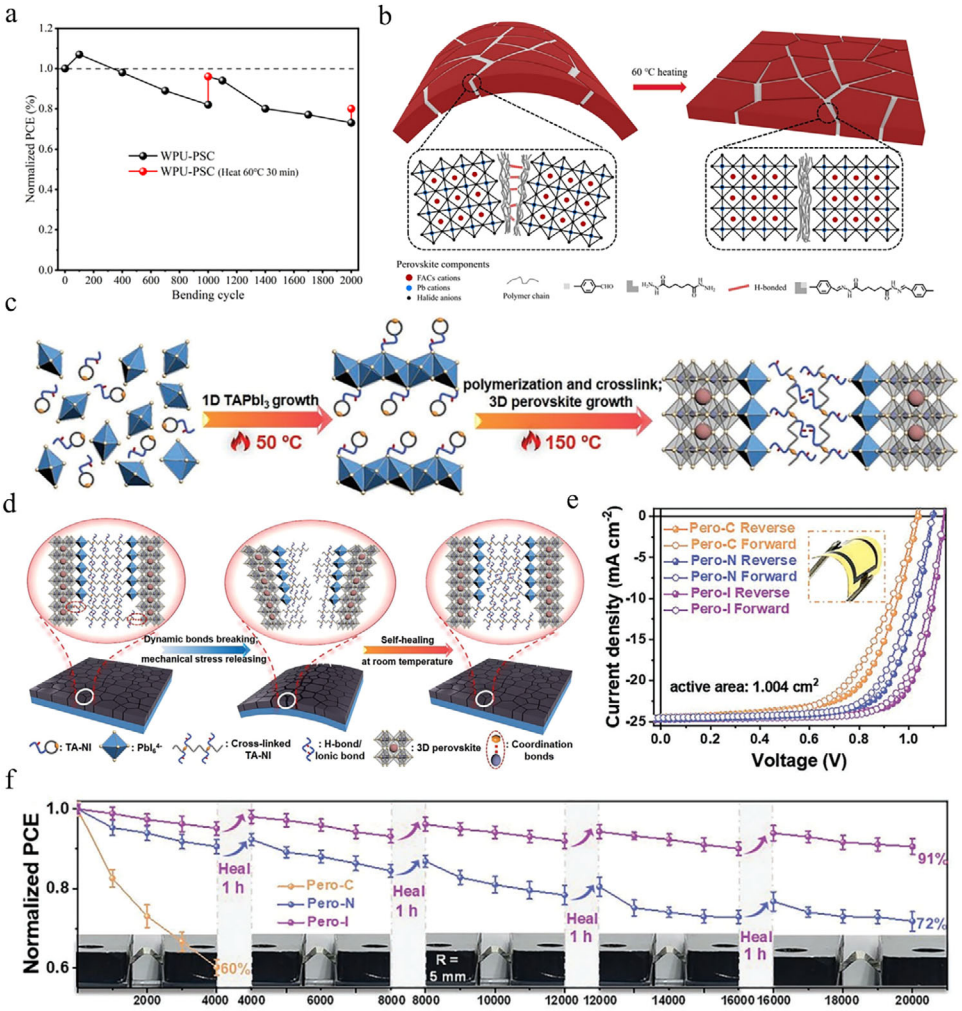

Figure 4. a) Bending resistance test of flexible perovskite solar cell devices treated with AB-WPU and efficiency test of device self-healing by heating at 1000 and 2000 bending cycles, respectively.[84] b) mechanism of Ab-WPU@perovskite membrane self-healing.[84] Copyright 2023, Royal Society of Chemistry. Schematic diagram of c) the formation of the grain-boundary "ligaments," and d) the self-healing process of Pero-I.[46] e) large-area (1.004 cm^2) flexible Pero-SCs based on Pero-C, Pero-N, and Pero-I under AM 1.5G, 100 mW cm^{-2} illumination. Inset: image of the devices.[46] f) Stability test of the unencapsulated flexible pero-SCs based on Pero-C, Pero-N, and Pero-I versus bending cycles at a radius of 5 mm.[46] Copyright 2023, Wiley-VCH GmbH.

recovery of optoelectronic properties (including carrier mobility and luminescence efficiency) occurs through dynamic ionic/vacancy migration and autonomous defect passivation. These findings underscore the critical importance of compositional engineering in enabling intrinsic self-repair in mixed-cation perovskite systems.

2.7. Robust Additive Functionalization

Benefiting from the intrinsic versatility of polymers, rational molecular design has enabled the integration of diverse additive strategies into self-healing perovskite solar cells (PSCs). These strategies aim to confine ion migration, prevent moisture ingress, alleviate mechanical stress, and enhance charge carrier transport.[102] Moreover, polymer-enabled self-healing primarily relies on dynamic chemical bonds such as isocyanate, disulfide, and carboxyl groups, which ensure device stability against both environmental factors and mechanical stresses through their reversible interactions.

A representative example involves the use of acylhydrazone-bonded waterborne polyurethane (Ab-WPU) as a dynamic covalent polymeric additive.[84] Owing to its relatively large molecular size, Ab-WPU does not infiltrate the perovskite lattice but selectively accumulates at grain boundaries, where it regulates crystallization and passivates charge-trapping defects. To validate Ab-WPU's self-healing function, flexible devices were subjected to bending cycles ranging from 100 to 2000 times. As illustrated in **Figure** 4a, while no efficiency loss occurred initially, increased bending induced more crack defects and progressive efficiency decline. After 1000 and 2000 bending cycles, heating at 60 °C for 30 min restored efficiency from 83% to 96% and from 73% to 80%, respectively. The underlying healing mechanism is illustrated in Figure 4b.[84] When exposed to sunlight,

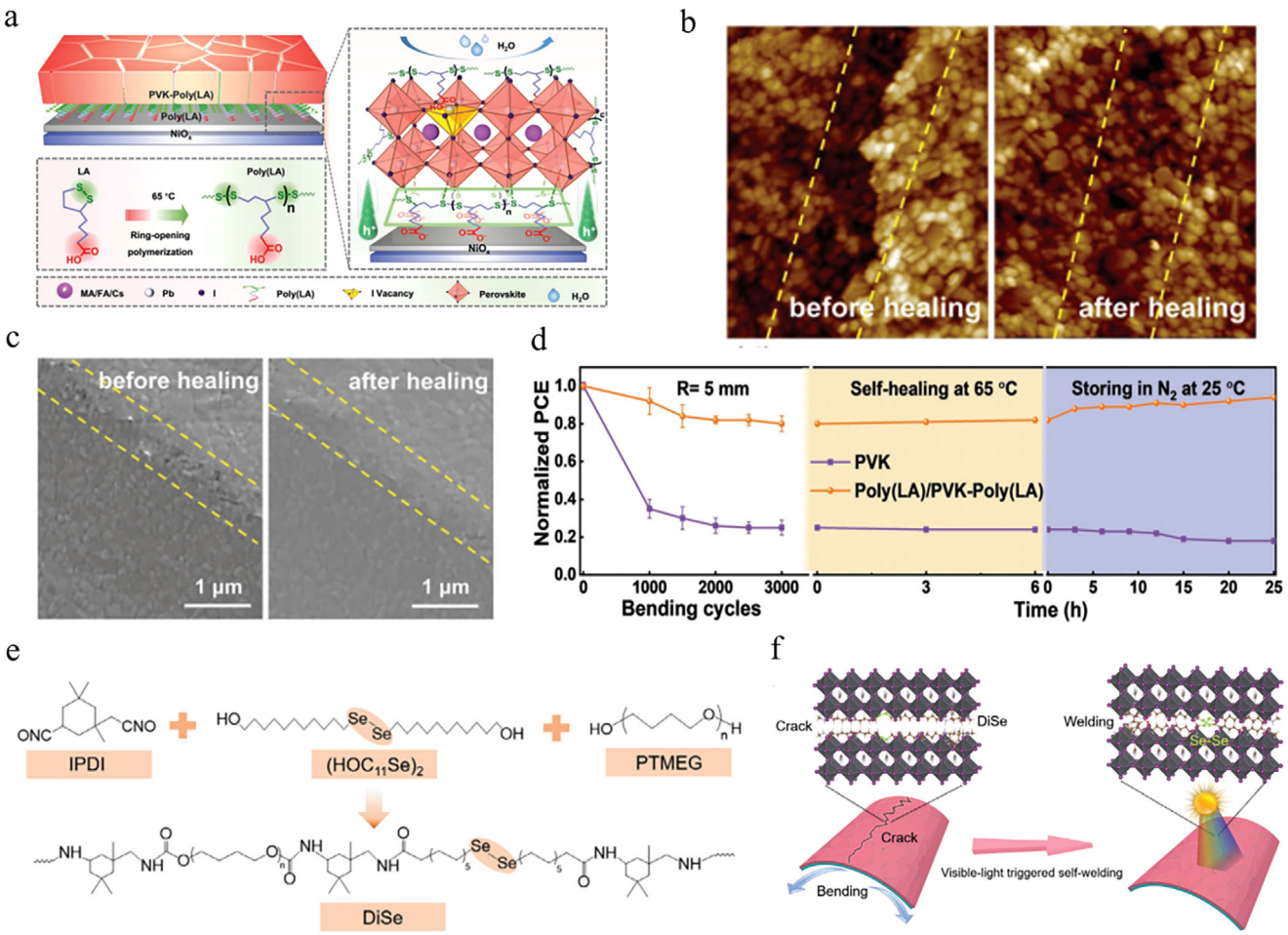

Figure 5. a) The thermal-initiated ring-opening polymerization of LA, and the schematic illustration of interface optimization and defect passivation mechanism via constructing an interpenetrating multifunctional cross-linked Poly(LA) network in PVSCs.[45] b) Atomic force microscopy (AFM) and c) SEM images of Poly(LA)/PVK-Poly(LA) film before and after the thermo-inducible self-healing.[45] d) The normalized PCE of flexible devices after different bending cycles at a curvature radius of 5 mm, subsequently self-healing at 65 °C for 6 h, and storing in N_2 at 25 °C for 25 h.[45] Copyright 2023, Wiley-VCH GmbH. e) Synthesis of DiSe.[104] f) Proposed visible-light-triggered self-welding mechanism involving dynamic diselenide bonds. Microstructure of perovskite films with micro-cracks.[104] Copyright 2024, Wiley-VCH GmbH.

Ab-WPU softens due to its viscoelastic properties, exhibiting greater stress absorption capacity than crystalline structures. This enhanced molecular mobility enables deformation and fractured resistance. Upon absorbing sufficient solar thermal energy, fracture surfaces dissociate into free aldehyde and hydrazine acylhydrazone groups. Concurrently, light exposure generates abundant free Pb^{2+} and I^- ions within the perovskite film. Stimulated by these ions, the acylhydrazone groups undergo reversible dynamic covalent bonding, enabling crack surface restoration.

Additionally, a crosslinkable monomer TA-NI, incorporating dynamic covalent disulfide bonds, hydrogen bonds, and ammonium groups, could function like reinforcing ligaments anchored at perovskite grain boundaries to crosslink the crystal structure.[46] As shown in Figure 4c,d, TA-NI initially coordinates with PbI_2 to form 1D $TAPbI_3$ during 50 °C annealing; subsequently, at 150 °C, TA-NI monomers simultaneously undergo crosslinking with elastic polymers while 3D perovskite crystals grow. This process yields a 1D/3D hybrid film where 1D $TAPbI_3$ adheres along 3D perovskite grain boundaries while TA-NI elastomers fill intergranular gaps. The elastomer's Lewis-basic sulfur atoms coordinate with uncoordinated Pb^{2+} ions, effectively dissipating mechanical stress within the perovskite film while enabling autonomous healing of bending-induced cracks in films at ambient temperature through its superior tensile properties. Hence, a high efficiency of 20.87%, with V_{oc} of 1.14 V, and *FF* of 0.74 was achieved for the 1.004 cm^2 Pero-I device (Figure 4e). Moreover, the device retains 93% of its initial PCE after 3000 h in a 30% relative humidity environment (Figure 4f), attributable to the dual-protection mechanism formed by the polymer and 1D structures that effectively block moisture penetration.

To enhance efficiency and mechanical robustness, a dual dynamic crosslinking network could be further engineered by incorporating naturally polymerizable α-lipoic acid (LA) molecules.[45] The schematic diagram of constructing a poly(LA) network for optimization and defect passivation is shown in **Figure 5a**. Upon mild thermal treatment, LA monomers undergo sequential crosslinking to form polymeric LA (denoted Poly(LA)). Poly(LA) primarily functions at grain boundaries and interfaces

between NiO_x and perovskite layers through its two key functional groups: disulfide (—S—S—) and carboxylic acid (—COOH). The carboxylic acid groups anchor onto NiO_x surfaces, passivating defects while preserving structurally beneficial Ni^{3+} species and reducing Ni^{4+} content, thereby improving electrical conductivity. Meanwhile, the oriented disulfide groups regulate perovskite crystal growth, yielding larger and more uniform grains that boost device PCE. Poly(LA)'s self-healing mechanism exploits its low melting transition (T_m),[103] which enables vigorous molecular motion to reconfigure broken hydrogen bonds and disulfide linkages under mechanical stress. After 3000 bending cycles at 5 mm radius, flexible devices retained 80% initial PCE. Subsequent mild thermal treatment at 65 °C effectively repaired cracks, with in situ AFM/SEM characterization (Figure 5b,c) revealing that healed films exhibited virtually indistinguishable perovskite grain compactness from pristine samples. Devices maintained 95% initial efficiency after 6 h at 65 °C (Figure 5d), demonstrating the defining impact of these dynamic bonds on flexible perovskite device bendability and recyclability.

A representative light-triggered self-healing strategy involves the use of a diselenide-based polymer (DiSe), synthesized from isophorone diisocyanate (IPDI), di-(1-hydroxyundecyl) diselenide $(HOC11Se)_2$, and polytetramethylene ether glycol (PTMEG).[104] This functional material preferentially localizes at perovskite film surfaces and grain boundaries, where it regulates crystal growth and effectively passivates defects (Figure 5e,f). Notably, the diselenide network enables crack repair through mild visible-light exposure, where mechanical stress-induced microcracks, caused by broken intramolecular interactions and diselenide bonds, are healed via dynamic bond rearrangement that crosslinks adjacent chains under illumination. SEM confirms effective crack bridging after 40 min light treatment. In situ PL characterization reveals a distinct redshift after 5000 bending cycles due to fractured coordinatively unsaturated sites, while progressive peak shifts toward shorter wavelengths during healing demonstrate Se atoms (generated from diselenide cleavage) compensating electron imbalance through high electron affinity. Concurrent diselenide bond exchange and rearrangement at fracture sites drive localized structural reconstruction around defects, ultimately restoring 92% initial PL intensity within 80 min under ambient conditions through this self-healing mechanism.

2.8. Dynamic Self-Healing Mechanisms

The dynamic self-healing exhibited by perovskite devices refers to their ability to spontaneously or partially/fully restore original structural and optoelectronic properties under mild conditions after defect formation (e.g., ionic vacancies, interstitial ions, grain boundary fractures) caused by external stimuli such as light, electric fields, humidity, and mechanical stress.[10] This capability is crucial for enhancing long-term stability in perovskite optoelectronic devices, including solar cells and LEDs.

A significant development in the field involves the design of ion-conductive elastomers (ICEs) featuring imidazolium-based ionic liquids. Leveraging the ionic liquid's high conductivity and the elastomer's dynamic covalent disulfide bonds, hydrogen bonds, and metal-coordination bonds, ICE demonstrates exceptional elasticity and electrical conductivity.[88] During self-healing, hydrogen bonds and coordination bonds first reform through non-covalent interactions to establish weak interfacial connections, followed by dynamic disulfide bond exchange along polymer chains that creates robust covalent interfaces to reconstruct the polymer network. As illustrated in **Figure 6a**, ICE exhibits remarkable stretchability with severed sections reconnecting within 3 min at room temperature. Electrical conductivity measurements (Figure 6b) confirm that ICE's conductivity across cut interfaces recovers within 1 s, demonstrating rapid self-healing. After 5000 bending cycles (3 mm radius), control films developed pronounced channel cracks and interfacial delamination, while ICE-incorporated films maintained structural integrity (Figure 6c). ICE devices retained >93% initial PCE after 10 000 bends (3 mm radius), and 80.3% after 10 000 bends (10 mm radius). Remarkably, after resting at 25 °C for 1 h, the latter recovered to 95% initial efficiency, whereas control devices suffered near-complete PCE degradation after 8000 bending cycles. These results unequivocally validate ICE's effectiveness in enabling dynamic self-healing for perovskite devices.

Additionally, one notable approach introduced 2-(1H-pyrazol-1-yl) pyridine (PZPY) into perovskite precursors to form 1D/3D hybrid structures.[44] HRTEM analysis revealed distinct crystallographic features (Figure 6d): the (200) planes of 3D perovskite exhibited an interplanar spacing (d-spacing) of 3.17 Å, while the (002) planes in 1D halide perovskite showed a d-spacing of 4.87 Å. In the 1D configuration, cations spontaneously self-assemble into optimally positioned linear octahedral arrangements. Conventional 3D perovskites feature corner-sharing $[PbX_6]^{4-}$ octahedra with A-site cations occupying interstitial cavities to form densely packed frameworks. PZPY molecules flanking the 3D perovskite reduce packing density, enhancing structural flexibility for self-healing. Crucially, $[PbI_6]^{4-}$ octahedra in 3D perovskites readily fragment into 2D layered/1D linear/0D quantum-confined configurations through metal–halide bond cleavage and structural reorganization. Device-generated heat accelerates A^+ cation vibrations within the octahedral framework, potentially ejecting A^+ groups from the lattice. This irreversible decomposition creates vacancy-related defects that degrade film stability. Accelerated testing under 55% RH with thermal cycling (25–85 °C) demonstrated stark contrasts (Figure 6e): unencapsulated control devices failed completely after 5 cycles, whereas 1D-3D devices maintained >90% initial efficiency despite varied thermal exposure durations (3–15 h at 85 °C), validating the dimensional hybridization strategy for operational stability.

A thermally responsive self-healing strategy was developed by Tang et al. through the synthesis of a hybrid disulfide framework (HDSF), obtained via dehydration–condensation of 4-aminophenyl disulfide (APD) and tris(4-formylphenyl)amine (TPA).[105] As illustrated in Figure 6f,g, the electron-donating atoms within HDSF's conjugated framework passivate undercoordinated Pb^{2+} sites on perovskite surfaces through coordination bonds, effectively suppressing undesirable secondary-phase PbI_2 formation. Primarily localized at perovskite surfaces and grain boundaries, HDSF stabilizes the crystal lattice against thermally induced distortion. At elevated temperatures (60–80 °C), dynamic disulfide exchange reactions within HDSF modulate thermal stress in perovskite crystals. This thermally triggered bond rupture/reorganization process enables self-healing by

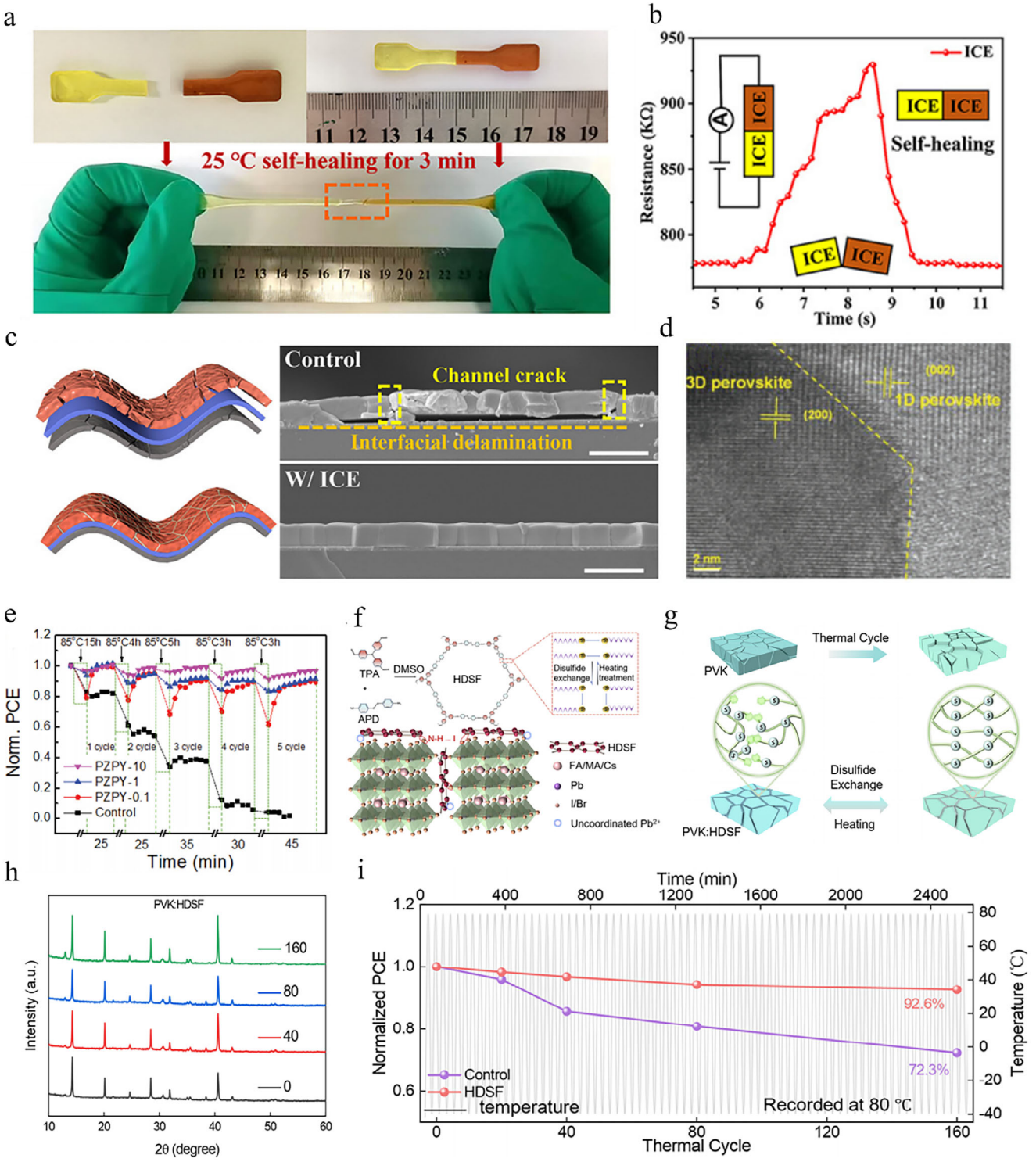

Figure 6. a) The cut ICE samples self-healed in 3 min at room temperature (25 °C). The red sample is the addition of $FeCl_3$ to ICE.[88] b) Resistance–time relationship before and after ICE cutting and its fast self-healing process.[88] c) Cross-sectional SEM images of the flexible PSCs tested for 5000 cycles (scale bar: 500 nm).[88] Copyright 2024, Royal Society of Chemistry. d) HRTEM image of 1D–3D heterostructure perovskite.[44] e) Long-term stability of the unencapsulated control and 1D–3D hybrid perovskite solar cells during temperature cycling (25–85 °C) at 55% RH.[44] Copyright 2018, Wiley-VCH Verlag GmbH & Co KGaA, Weinheim. f) Schematic illustration of the interaction mechanism between HDSF and perovskite crystals, including the heat-triggered dynamic exchange process of the disulfide bond.[105] g) Schematic illustration of heat-triggered self-healing properties via dynamic exchange of disulfide bonds in HDSF.[105] The XRD evolution of h) HDSF-treated perovskite films during thermal cycle tests.[105] i) Cycling stability recorded at 80 °C of control and HDSF-treated devices against thermal cycles between −40 and +80 °C.[105] Copyright 2025, Wiley-VCH GmbH.

dynamically regulating thermomechanical stress across varying temperatures. During thermal cycling (20 °C min^{-1} ramp rate: RT→80 °C→−40 °C→RT), XRD analysis (Figure 6h) revealed excessive PbI_2 formation in control samples after 160 cycles, accelerating perovskite decomposition under photo-thermal stress. In contrast, HDSF-treated films maintained significantly lower PbI_2 content. Device stability testing (Figure 6i) demonstrated severe degradation in control, retaining merely 72.3% of its initial PCE at 80 °C after 160 cycles. Remarkably, HDSF-modified devices preserved 92.6% initial efficiency, confirming enhanced structural integrity through dynamic disulfide reorganization.

These representative studies collectively underscore the versatility and efficacy of dynamic self-healing strategies in perovskite optoelectronic devices. By harnessing reversible interactions, including hydrogen bonding, metal coordination, and dynamic covalent exchange (e.g., disulfide and diselenide bonds), researchers have engineered functional materials that can withstand mechanical deformation, thermal cycling, and prolonged operational stress. These dynamic networks not only suppress the accumulation of defects and alleviate structural fatigue but also actively enable the restoration of optoelectronic properties under ambient or mildly elevated temperatures. Notably, the integration of self-healing functionalities has been shown to preserve, and in many cases enhance, long-term device performance without compromising initial efficiency. As research advances, integrating dynamic healing frameworks with scalable fabrication techniques and encapsulation strategies will be critical to realizing commercially viable, resilient perovskite optoelectronics.

2.9. Operando/Multimodal Evidence

To quantitatively assess the self-healing capabilities of perovskite materials, researchers employ a suite of characterization techniques. These methods are crucial for monitoring the degradation and subsequent recovery of key properties.

In the study of self-healing strategies, understanding the diverse crosslinking mechanisms often requires tracking elemental migration, making ToF-SIMS a vital technique for visualizing chemical composition and elemental distribution. To examine whether crosslinking mechanisms observed in bulk solutions can be replicated in solid thin films, Li et al. employed ToF-SIMS and observed a gradient distribution of S atoms from TA-NI throughout the 3D perovskite film (**Figure** 7a), indicating successful diffusion of TA-NI across the entire layer.[46] Complementary GIWAXS (Figure 7b,c) analysis further revealed the formation of a 1D $TAPbI_3$ perovskite phase in the Pero-I sample, in addition to the characteristic 3D perovskite diffraction peaks from (110), (012), and (220) planes, confirming the effective functioning of the crosslinking agent within the film.

Beyond elemental and crystallographic changes, 2D XRD has demonstrated the enhancement of film stability through self-healing strategies. Chen et al. used 2D XRD (Figure 7d,e) to show that under repeated bending at a 5 mm radius, the reference perovskite film suffered from grain detachment, leading to significantly weakened diffraction intensity and the emergence of substrate signals near 26°.[45] In contrast, the self-healing poly(LA) network maintained nearly unchanged diffraction peak intensity after bending.

PL imaging offers intuitive insights into how defects and phase segregation impact device performance, enabling better evaluation of self-healing approaches. Wang et al. performed 2D PL mapping (Figure 7g,h) and found that after 8 h of irradiation, the control film exhibited a substantial drop in PL intensity due to accumulated light-induced defects, accompanied by a redshift of the emission peak from 800.8 nm to 806.7 nm, along with gradual formation of δ-phase domains.[104] In contrast, the DiSe-based self-healing device showed only a minor PL peak shift from 800.2 to 801.4 nm. ToF-SIMS further confirmed severe A-site cation migration and inhomogeneous distribution in the control film after light exposure (Figure 7f), collectively underscoring the efficacy of the self-healing strategy.

By integrating multiple characterization techniques, multimodal analysis provides a comprehensive picture of the dynamic interrelationships among elemental migration, structural reorganization, and functional recovery during the self-healing process in perovskites. This approach moves beyond the limitations of single-technique studies, elevating phenomenological observations to mechanistic understanding and offering an essential holistic perspective and quantitative foundation for the precise design and optimization of new-generation perovskite materials with robust self-healing capabilities.

2.10. Scalable Applications

The scalable application of self-healing perovskite technology is accelerating its transition from fundamental research to industrial implementation. Its core value lies in addressing the degradation of perovskite materials under mechanical stress, environmental erosion, and thermal cycling through dynamic bond reorganization, bio-inspired structural design, and intelligent material integration-thereby significantly extending device lifespan while reducing maintenance costs.

Under natural light conditions, light–dark cycles can cause irreversible ion migration in perovskite solar cells, which poses a significant challenge to the long-term outdoor operational stability of the cells. The daytime stability of perovskite solar modules could be enhanced by isolating the defective octahedrons on the perovskite surface using vapor-deposited multidentate ligands.[90] Even after 101 light–dark cycles at 50 °C, the modules retained over 97% of their initial efficiencies. The concept of perovskite surface octahedron isolation is illustrated in **Figure** 8a. Pre-formed $FAPbI_3$ perovskite films were treated with vapor-deposited 2,2′:6′,2″-terpyridine (Tpy), a multidentate ligand that forms a 0D framework $(Tpy)_2PbI_6$ when mixed with PbI_2. Density functional theory (DFT) calculations revealed that after surface octahedron isolation treatment, the formation energy of most typical defects near the perovskite surface increased (Figure 8b). The activation energy for ion migration (Figure 8c) in the isolated samples (0.68 eV) was significantly higher than that in the pristine samples (0.43 eV), indicating that ion migration was effectively suppressed in the perovskite films subjected to surface octahedron isolation treatment. A large-area module with an aperture area of 785 cm^2 was fabricated as a representative device (Figure 8d) to evaluate its photovoltaic properties, and day–night cycle aging tests were conducted as shown in Figure 8e. The pristine module retained only ≈55% of its initial PCE after 20

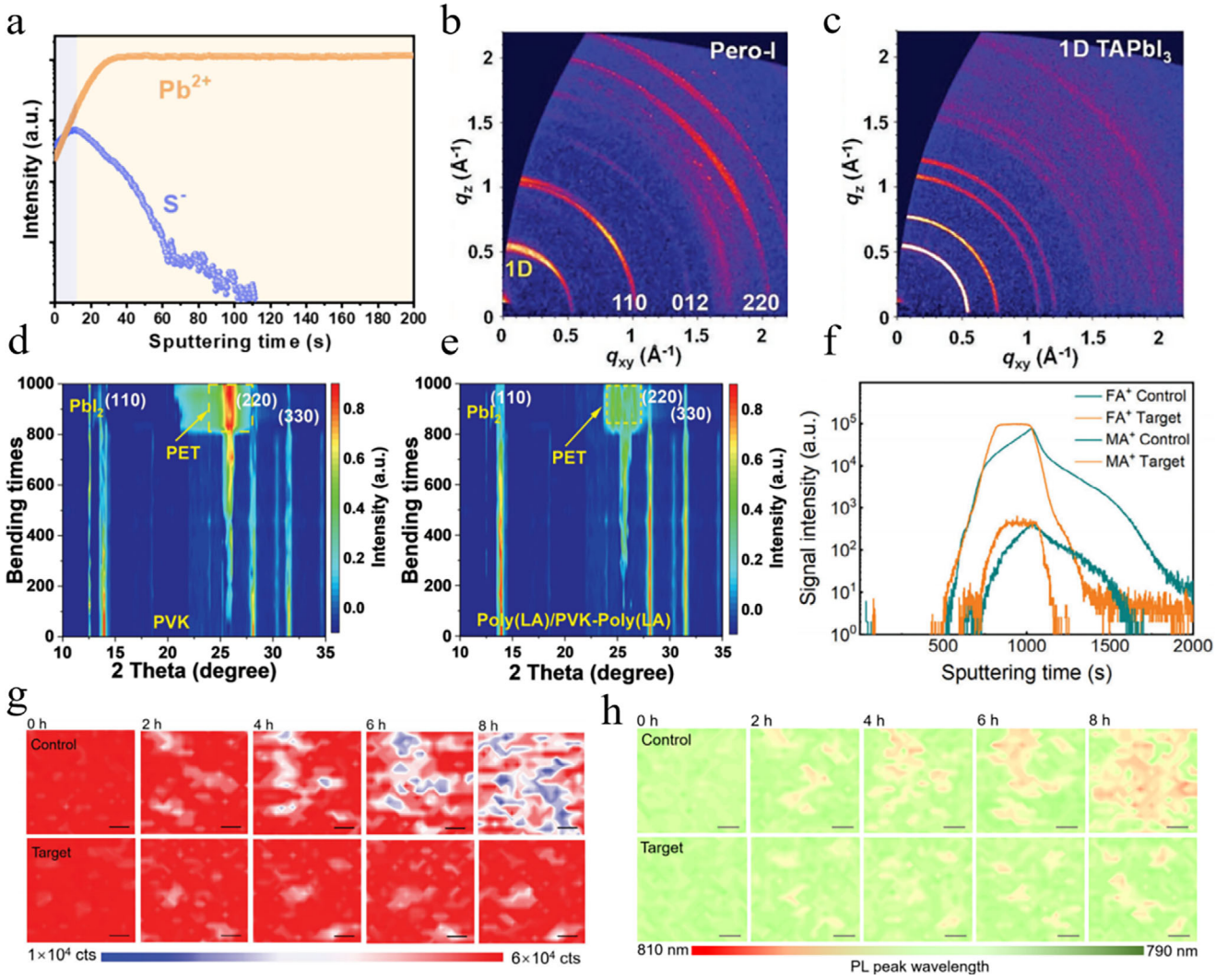

Figure 7. a) ToF-SIMS depth profiles of Pb^{2+} and S- sputtering from top to bottom for the Pero-I film.[46] b) 2D GIWAXS patterns of Pero-I and c) 1D $TAPbI_3$.[46] Copyright 2023, Wiley-VCH GmbH. d,e) 2D XRD patterns of PVK and Poly(LA)/PVK-Poly(LA) films measured with continuous bending from 0 to 1000 cycles.[45] Copyright 2023, Wiley-VCH GmbH. f) ToF-SIMS depth profiles of the FA^+ and MA^+ cation distribution in the control and target F-PSCs under continuous light illumination at 50 °C over 8 h.[104] In situ 2D PL mapping spectra of g) peak intensity; h) peak position, evolution of the perovskite films under light illumination over 8 h in the air a with a relative humidity of 40%. Scale bar = 1 μm.[104] Copyright 2024, Wiley-VCH GmbH.

light–dark cycles, while the isolated module exhibited reversible PCE loss and even retained over 97% of its initial PCE after 101 light–dark cycles at 50 °C, suggesting that the surface octahedron isolation strategy inhibited irreversible degradation during light–dark cycles. Subsequently, the reliability of the solar modules was evaluated under real outdoor conditions using a multilayer encapsulation technique. As shown in Figure 8f, the performance decreased from morning to noon and then slightly recovered from noon to evening, demonstrating reversible performance recovery overnight and outdoor stability comparable to that of commercial Si solar cells. This not only improves the mechanistic understanding of mobile ionic defects that cause irreversible device degradation but also promotes the advancement of perovskite devices capable of meeting the demands of real-world applications.

To address challenges in both small-area solar cells and large submodules, Zhao et al. developed an impurity-healing interface engineering strategy.[91] By introducing functional cations (2-(1-cyclohexenyl)ethylammonium iodide, CHEAI) on $FAPbI_3$, they constructed a high-mobility 2D perovskite layer that effectively converts excess PbI_2 and residual yellow-phase δ-$FAPbI_3$ impurities into low-dimensional perovskite phases at 3D perovskite surfaces and grain boundaries. GIWAXS measurements (Figure 8g,h) revealed the disappearance of impurity signals in CHEAI-treated samples, with new signals emerging at q ≈3.7 nm^{-1} indicating transformation of impurities into low-dimensional perovskite. The CHEAI treatment simultaneously heals grain boundaries and pin holes while penetrating crystal interfaces for comprehensive defect healing (Figure 8i,j). After CHEAI treatment, the devices achieved a high PCE of 25.86% while maintaining 92% of their initial efficiency after 1500 h of maximum power point tracking (MPPT). Scaling device area exacerbates perovskite film inhomogeneity issues, but PL intensity

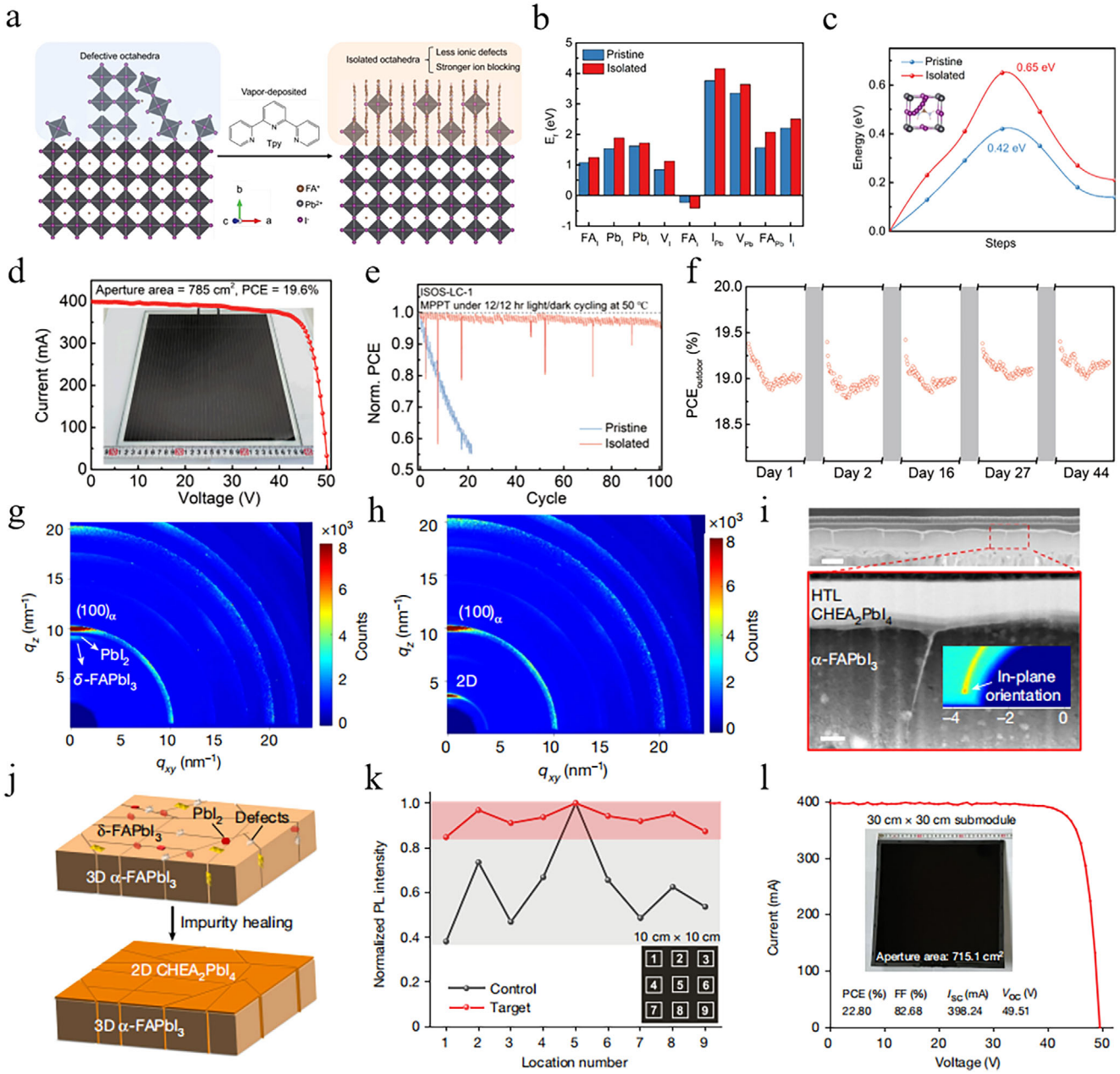

Figure 8. a) Schematic illustration of perovskite surface octahedra isolation.[90] b) Formation energies of nine neutral point defects in perovskite surfaces, including two vacancies (V_{Pb}, V_I), three interstitials (Pb_i, I_i, and FA_i), and four antisites (Pb_I, I_{Pb}, I_{FA}, and Pb_{FA}).[90] c) Calculated minimum energy pathways for iodide ion migration in pristine and isolated $FAPbI_3$. The inset shows the migration pathway.[90] d) I–V characteristics of the champion solar modules with an aperture area of 785 cm^2, whereas the active area (electrically functional portion) measures 730 cm^2.[90] e) Normalized PCE.[90] f) Diurnal variation of PCE outdoor for perovskite modules over 5 days, recorded from 7 a.m. to 7 p.m.[90] Copyright 2025, The American Association for the Advancement of Science. GIWAXS patterns of g) control and h) target films.[91] i) Cross-sectional HR-STEM images of a target PSC sample. Scale bars, 500 nm (above); 100 nm (below).[91] j) Schematic of the CHEAI-induced impurity-healing process.[91] k) Normalized PL intensity of 10 × 10 cm^2 perovskite films when measured at different positions.[91] l) *J–V* curve of the champion 30 × 30 cm^2 target PSM and photograph (inset) of a 30 × 30 cm^2 PSM.[91] Copyright 2024, Haifei Wang et al, under exclusive licence to Springer Nature Limited.

mapping on 10 × 10 cm^2 devices (Figure 8k) demonstrates that CHEAI treatment effectively compensates for non-uniformity in large-area films, exhibiting significantly reduced PL variation. Ultimately, CHEAI-treated 30 × 30 cm^2 large-area modules (active area 715.1 cm^2) (Figure 8l) reached 22.80% PCE (certified 22.46%) and retained 94% initial efficiency after 528 h thermal aging at 65 °C, demonstrating substantial stability enhancement through impurity-healing engineering.

Inspired by the integration of pangolin's rigid scales and soft body tissue, Lee et al. developed a bio-inspired structural design for self-healing flexible PeLEDs.[106] This approach employs a polymer-assisted crystallization modulation strategy

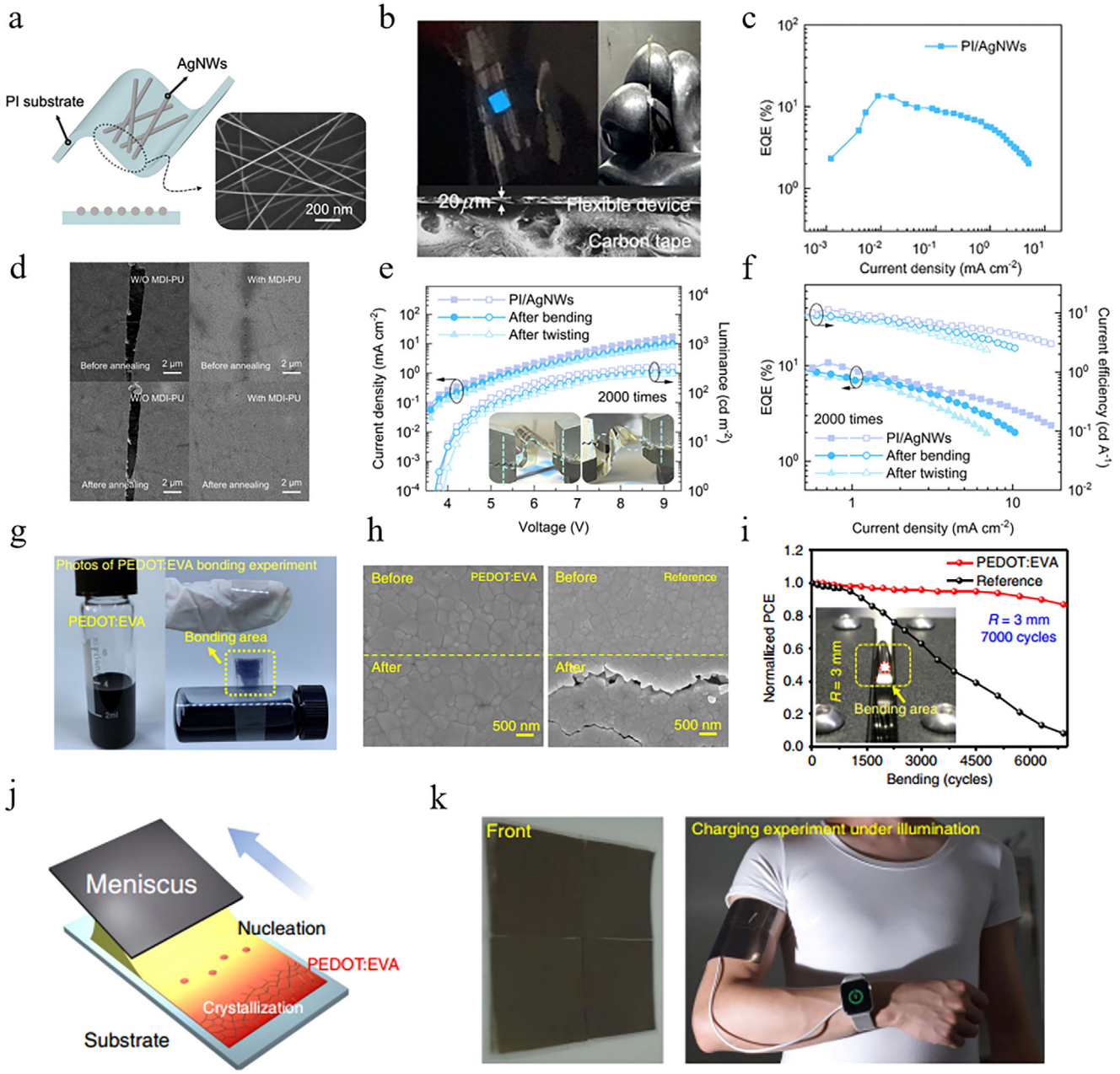

Figure 9. a) Schematic illustration and the SEM image of PI/AgNW substrate.[106] b) Photographs of flexible devices.[106] c) EQE as a function of current density.[106] d) SEM images of mechanical cracks in perovskite films without and with MDI-PU before and after annealing treatment, respectively.[106] e) *J–V–L* characteristics. Insets are the photographs of the bending test and twisting test setups.[106] f) EQE and current efficiency as a function of current density measured after repeated bending and twisting.[106] Copyright 2022, American Chemical Society. g) Photographs of PEDOT:EVA bonding experiment.[107] h) SEM images for the perovskite films before and after bending.[107] i) Normalized averaged PCE value for the flexible PSCs as a function of bending cycles with a radius of 3 mm.[107] j) Schematic of PSCs by meniscus-coating.[107] k) Photographs of flexible perovskite solar modules as a wearable power source.[107] Copyright 2020, Meng et al.

using diphenylmethane diisocyanate polyurethane (MDI-PU) soft elastomers. To fully realize the potential of flexible PeLEDs, silver nanowires (AgNWs) were adopted to replace brittle ITO electrodes. As illustrated in **Figure** 9a,b, the schematic of the PI/AgNW electrode and SEM images of AgNWs embedded in PI substrate after detachment from glass confirm the exceptional mechanical flexibility of the ultrathin PI/AgNW composite electrode. Notably, both electrical resistance and transmittance remained virtually unchanged after 50 000 cycles of high-intensity stress tests involving bending and twisting. The resulting sky-blue flexible PeLEDs fabricated on ultrathin (20 μm) PI/AgNW electrodes with MDI-PU assistance achieved a peak external quantum efficiency (EQE) of 13.5% (Figure 9c), among the highest reported values for sky-blue flexible PeLEDs. Comparative

SEM (Figure 9d) images demonstrate the self-healing process of perovskite films with/without MDI-PU: MDI-PU-incorporated films exhibited significant crack repair under thermal treatment. After 2000 bending–twisting cycles (Figure 9e,f), the flexible PeLEDs retained 87.8% and 80.7% of their initial EQE values. This AgNW-based flexible transparent electrode substantially enhanced both the crystallinity of perovskite films on plastic substrates and resistance to bending strain.

Considering the robust crystalline structure and flexible connections of vertebrae, a conductive adhesive polymer, such as PEDOT:EVA, between the ITO and perovskite layers, could act as cartilage between vertebral bodies.[107] Due to its elasticity and adhesion, this layer uniformly distributes force and expands the support area, simultaneously promoting directional crystallization of perovskite and enhancing device adhesion. As shown in adhesion tests of PEDOT:EVA (Figure 9g), this layer precisely controls nucleation sites and crystal orientation growth in high-quality flexible perovskite films. It promotes film crystallization, significantly increases overall grain size, and reduces surface roughness. The PEDOT:EVA layer effectively lowers carrier defect concentrations on both top and bottom surfaces, substantially optimizing the pairing between surface and bulk defects caused by thermodynamic instability during annealing and reducing non-radiative recombination losses. To demonstrate PEDOT:EVA's adhesion, SEM images (Figure 9h,i) of perovskite films after 7000 bending cycles (3 mm radius) show no visible cracks on PEDOT:EVA-based films, maintaining 85% of initial efficiency. Additionally, high-quality large-area perovskite films were prepared via meniscus coating technology, with a module comprising four sub-cells (36 cm^2) shown in Figure 9j,k. This establishes the feasibility of low-power devices.

Tandem architectures, which combine wide-bandgap (WBG) and narrow-bandgap (NBG) sub-cells, are designed to surpass the efficiency limit of single-junction solar cells. However, their complex structure introduces unique stability challenges, placing greater demands on self-healing technologies.

In two-terminal (2-T) tandems, the two subcells are connected via a recombination layer or tunnel junction. The performance and durability of this interlayer represent a core challenge for self-healing design. Drawing inspiration from strategies used in other self-healing systems, one can consider incorporating dynamic chemical bonds, such as dynamic covalent bonds (e.g., disulfide bonds, boronic ester bonds) or strong reversible non-covalent interactions (e.g., ionic coordination bonds, hydrogen-bonding networks), at this interface. These bonds can repair damage when the device is subjected to heat or minor strain, preventing interfacial delamination and maintaining low recombination resistance. Furthermore, the current in a 2-T tandem is limited by the less efficient sub-cell. This requires highly synchronized degradation rates and post-repair performance recovery between the two sub-cells.[108,109] If one sub-cell is fully restored while the other degrades significantly, the overall efficiency will not improve. This necessitates a holistic, system-level approach to self-healing design.

In three-terminal (3-T) tandem structures, the two sub-cells are connected optically and electrically in parallel through a shared middle electrode. This electrode must exhibit high transparency and excellent conductivity, and both the electrode itself and its interfaces with adjacent functional layers should possess self-healing capability. For instance, when conductive pathways break due to repeated bending, a self-healing polymer matrix could enable reconnection and restore conductivity.[110] A key advantage of the 3-T configuration is the ability to manage and repair the sub-cells relatively independently. The WBG sub-cell, often containing bromine, is primarily prone to halogen phase segregation. Repair strategies should therefore focus on introducing additives that anchor halide ions, thereby enhancing lattice stability.[111,112] In contrast, common NBG cells face the challenge of Sn^{2+} oxidation to Sn^{4+}. Sn^{4+} acts not only as a p-type dopant, increasing device leakage current, but also as a deep-level defect that induces severe non-radiative recombination.[113,114] A promising self-healing approach involves designing functional interlayers or additives that establish a dynamic Sn^{4+}/Sn^{2+} redox cycle, where a healing agent reversibly reduces Sn^{4+} back to Sn^{2+}, enabling real-time defect repair.[115,116]

In addition to these targeted strategies, general self-healing mechanisms remain essential for repairing grain boundaries and mitigating halide segregation, ensuring the development of multifunctional and renewable self-healing systems that safeguard device performance and long-term stability.

After decades of refinement, semiconductor technology has become capable of withstanding multiple stressors in the space environment. These include harsh conditions such as ionizing and non-ionizing radiation, thermal cycling, and vacuum conditions. With the continuous increase in low-Earth orbit satellites, perovskite, as a new generation of solar cell technology offering superior cost and weight advantages over traditional spacecraft solar cells, can play a role in the burgeoning space economy.

Regarding the application of self-healing technologies in scalable, high-stress scenarios such as space and High-Altitude Long-Endurance (HALE) platforms, future research must pivot from fundamental material discovery toward engineered system-level solutions. These environments present a confluence of extreme stressors, intense ultraviolet and particle radiation, drastic thermal cycling (e.g., from −80 to 80 °C), and mechanical stress from low-quality or degraded encapsulation. To address these, self-healing strategies must be designed for autonomy and efficiency under low-energy triggers. For instance, the inherent thermal energy from the day-night cycle, rather than being solely a degradation driver, can be harnessed as a built-in, periodic trigger for self-repair. This involves developing perovskite compositions and composite matrices (e.g., with tailored polymers or low-glass-transition-temperature additives) where thermal fluctuations actively promote the re-crystallization of damaged grains and the re-migration of halide ions, effectively "resetting" the device at each cycle. Additionally, under high-energy radiation, energetic particles transfer energy to atoms within the perovskite lattice, leading to the formation of Frenkel pairs and inducing secondary displacements. The relatively weaker and more ionic character of bonding at the A-site facilitates the dissociation and subsequent recombination of cations under ionization radiation. Owing to the low migration energy barriers of ionic species in perovskites, radiation-induced defects can be effectively deactivated, contributing to the material's inherent radiation tolerance.[117,118] However, under sustained or intense radiation flux, excessive defect generation, such as through proton irradiation, may surpass the intrinsic self-healing capacity of the material, thereby compromising long-term operational reliability. It is therefore

essential to establish systematic mechanisms, such as compositional engineering, interface modulation, or the incorporation of dynamic bond-forming additives, to enhance defect tolerance and ensure consistent self-recovery under extreme conditions.[119–121] The key opportunities are profound: achieving unprecedented durability with thinner, lighter, and more flexible modules, a critical advantage for reducing launch mass for space missions or increasing payload for HALE platforms. Furthermore, by mitigating the impact of inevitable micro-cracks and pinhole defects in low-quality encapsulation, self-healing can dramatically lower the bar for packaging requirements, reducing system cost and complexity. However, significant limitations must be overcome. The primary challenge is ensuring that the self-healing mechanism does not compromise the initial peak efficiency and possesses a sufficient "healing budget," a finite number of repair cycles before the material is exhausted. The long-term chemical stability of healing agents (e.g., mobile halide reservoirs or dynamic bonding molecules) under continuous operation and the potential for unintended side-reactions at interfaces are critical concerns. Therefore, future research should be guided by a focus on: i) developing wide-temperature-range, moisture-insensitive healing chemistries; ii) integrating multi-modal, in situ characterization (e.g., with PL, XRD, SIMS) into environmental testing chambers to directly observe repair dynamics under simulated operational stresses; and iii) establishing accelerated life-testing protocols that specifically account for and quantify the cyclic healing–degradation–healing lifecycle. The ultimate goal is to transition self-healing from a fascinating laboratory phenomenon into a reliable, predictable, and scalable engineering feature for the harshest operational environments.

3. Conclusion and Outlook

In this review, we summarized key advances in self-healing PSCs. Initiating degradation mechanisms, we analyzed perovskite breakdown under environmental stressors (light/moisture/heat) and intrinsic processes like ion migration and defect formation. Distinguishing irreversible from reversible degradation pathways provides fundamental insights for designing self-healing PSCs. We then systematically examined three strategic approaches: composition engineering, robust network incorporation, and dynamic bonding systems. Each was evaluated through detailed case studies of their healing mechanisms and impact on PSC stability, particularly regarding performance retention during rigorous flexural endurance testing (5000–10000 bending cycles) and thermal cycling (−40 °C↔85 °C).

Self-healing approaches for PSCs have now evolved from niche research concepts to promising stability-enhancement platforms with practical relevance. By leveraging reversible chemical bonds, ionic migration control, and dynamic network architectures, researchers have achieved significant improvements in mechanical resilience, moisture tolerance, and thermal stability.

However, current research on self-healing perovskites still faces several limitations. First, many efficient self-healing mechanisms rely on the incorporation of long-chain polymers, which can repair damage through segmental motion. However, most of these polymers are electrically insulating and may exhibit energy level misalignment with perovskites. This can create barriers at grain boundaries, hindering charge carrier extraction and transport, thereby compromising device efficiency. Future studies should focus on balancing self-healing capability with optoelectronic performance through strategies such as molecular structure optimization, spatial distribution control, and trigger condition refinement. Moreover, existing self-healing research predominantly focuses on short-term performance testing, with limited exploration of its potential under real-world operating conditions. Several critical questions remain unanswered: whether the healing efficacy can be maintained optimally as healing agents are depleted, dynamic bonds fatigue, or byproducts accumulate; whether the healing mechanism itself can remain stable under long-term external stimulation; and whether the device's optoelectronic performance can be sustained at a high level after numerous healing cycles. These aspects represent key directions for future in-depth investigation.

Looking forward, we believe the next stage of development will require:

i. Scalability: integration of healing functionalities into roll-to-roll, slot-die, or other continuous manufacturing processes to enable large-area module production.
ii. Multi-trigger responsiveness: designing materials responsive to combinations of light, heat, and electrical bias for adaptive, on-demand healing under real-world operating conditions.
iii. System-level integration: embedding self-healing PSCs into flexible electronics, tandem architectures, and building-integrated photovoltaic (BIPV) systems to broaden application potential.
iv. Predictive design: utilizing computational modeling and machine learning to forecast degradation-healing cycles and optimise healing chemistries for specific deployment environments.

By aligning fundamental advances with scalable manufacturing and system-level integration, defect-healing-enabled PSCs can transition from laboratory prototypes to robust, high-efficiency, and commercially viable renewable energy technologies.

Acknowledgements

This work was supported by Southeast University. The authors acknowledge financial support from the Start-up Fund of Southeast University. Q. Cao acknowledges the support from the Society of Science Fellows Postdoctoral Fellowship at the University of Notre Dame.

Conflict of Interest

The authors declare no conflict of interest.

Keywords

defect-healing approaches, degradation mechanisms, environmental stressors, operational stability, perovskite solar cells

Received: September 3, 2025
Revised: October 13, 2025
Published online: October 24, 2025

[1] X. Luo, X. Lin, F. Gao, Y. Zhao, X. Li, L. Zhan, Z. Qiu, J. Wang, C. Chen, L. Meng, X. Gao, Y. Zhang, Z. Huang, R. Fan, H. Liu, Y. Chen, X. Ren, J. Tang, C.-H. Chen, D. Yang, Y. Tu, X. Liu, D. Liu, Q. Zhao, J. You, J. Fang, Y. Wu, H. Han, X. Zhang, D. Zhao, et al., *Sci. China Chem.* **2022**, *65*, 2369.
[2] J. Zhou, L. Tan, Y. Liu, H. Li, X. Liu, M. Li, S. Wang, Y. Zhang, C. Jiang, R. Hua, W. Tress, S. Meloni, C. Yi, *Joule* **2024**, *8*, 1691.
[3] L. Shen, P. Song, K. Jiang, L. Zheng, J. Qiu, F. Li, Y. Huang, J. Yang, C. Tian, A. K. Y. Jen, L. Xie, Z. Wei, *Nat. Commun.* **2024**, *15*, 10908.
[4] S. Gong, G. Qu, Y. Qiao, Y. Wen, Y. Huang, S. Cai, L. Zhang, K. Jiang, S. Liu, M. Lin, M. C. Beard, Z.-X. Xu, X. Chen, *Energy Environ. Sci.* **2024**, *17*, 5080.
[5] P. Fu, D. Yang, Y. Chen, R. Lu, M. A. Haque, Y. Liu, Y. Han, H. Li, R. Chen, J. Liu, W. Qin, L. H. Hernandez, F. Fan, K. Wu, D. Baran, H. Zhou, C. Li, *Energy Environ. Sci.* **2025**, *18*, 7082.
[6] H. Chen, Q. Wei, M. I. Saidaminov, F. Wang, A. Johnston, Y. Hou, Z. Peng, K. Xu, W. Zhou, Z. Liu, L. Qiao, X. Wang, S. Xu, J. Li, R. Long, Y. Ke, E. H. Sargent, Z. Ning, *Adv. Mater.* **2019**, *31*, 1903559.
[7] H. Chen, C. Liu, J. Xu, A. Maxwell, W. Zhou, Y. Yang, Q. Zhou, A. S. R. Bati, H. Wan, Z. Wang, L. Zeng, J. Wang, P. Serles, Y. Liu, S. Teale, Y. Liu, M. I. Saidaminov, M. Li, N. Rolston, S. Hoogland, T. Filleter, M. G. Kanatzidis, B. Chen, Z. Ning, E. H. Sargent, *Science* **2024**, *384*, 189.
[8] C. Liu, Y. Yang, H. Chen, J. Xu, A. Liu, A. S. R. Bati, H. Zhu, L. Grater, S. S. Hadke, C. Huang, V. K. Sangwan, T. Cai, D. Shin, L. X. Chen, M. C. Hersam, C. A. Mirkin, B. Chen, M. G. Kanatzidis, E. H. Sargent, *Science* **2023**, *382*, 810.
[9] Y. Zhang, Q. Song, G. Liu, Y. Chen, Z. Guo, N. Li, X. Niu, Z. Qiu, W. Zhou, Z. Huang, C. Zhu, H. Zai, S. Ma, Y. Bai, Q. Chen, W. Huang, Q. Zhao, H. Zhou, *Nat. Photonics.* **2023**, *17*, 1066.
[10] F. Huang, L. Jiang, A. R. Pascoe, Y. Yan, U. Bach, L. Spiccia, Y.-B. Cheng, *Nano Energy* **2016**, *27*, 509.
[11] K. Domanski, B. Roose, T. Matsui, M. Saliba, S.-H. Turren-Cruz, J.-P. Correa-Baena, C. R. Carmona, G. Richardson, J. M. Foster, F. De Angelis, J. M. Ball, A. Petrozza, N. Mine, M. K. Nazeeruddin, W. Tress, M. Grätzel, U. Steiner, A. Hagfeldt, A. Abate, *Energy Environ. Sci.* **2017**, *10*, 604.
[12] Z. Shen, Q. Han, X. Luo, Y. Shen, Y. Wang, Y. Yuan, Y. Zhang, Y. Yang, L. Han, *Nat. Photonics.* **2024**, *18*, 450.
[13] W. Nie, J. C. Blancon, A. J. Neukirch, K. Appavoo, H. Tsai, M. Chhowalla, M. A. Alam, M. Y. Sfeir, C. Katan, J. Even, S. Tretiak, J. J. Crochet, G. Gupta, A. D. Mohite, *Nat. Commun.* **2016**, *7*, 11574.
[14] E. Bi, H. Chen, F. Xie, Y. Wu, W. Chen, Y. Su, A. Islam, M. Grätzel, X. Yang, L. Han, *Nat. Commun.* **2017**, *8*, 15330.
[15] J. Liang, X. Hu, C. Wang, C. Liang, C. Chen, M. Xiao, J. Li, C. Tao, G. Xing, R. Yu, W. Ke, G. Fang, *Joule* **2022**, *6*, 816.
[16] Y. Yun, Q. Chang, J. Yan, Y. Tian, S. Jiang, W. Wei, S. Li, Y. Guo, J. Yin, J. Li, M. Chen, K. Huang, C. Li, R. Zhang, *Sci.Adv* **2025**, *11*, adp3112.
[17] K. Ho, M. Wei, E. H. Sargent, G. C. Walker, *ACS Energy Lett.* **2021**, *6*, 934.
[18] W. Tress, N. Marinova, T. Moehl, S. M. Zakeeruddin, M. K. Nazeeruddin, M. Grätzel, *Energy Environ. Sci.* **2015**, *8*, 995.
[19] Q. Jiang, R. Tirawat, R. A. Kerner, E. A. Gaulding, Y. Xian, X. Wang, J. M. Newkirk, Y. Yan, J. J. Berry, K. Zhu, *Nature* **2023**, *623*, 313.
[20] T. Liu, X. Zhao, X. Zhong, Q. C. Burlingame, A. Kahn, Y.-L. Loo, *ACS Energy Lett.* **2022**, *7*, 3531.
[21] G. Nazir, S.-Y. Lee, J.-H. Lee, A. Rehman, J.-K. Lee, S. I. Seok, S.-J. Park, *Adv. Mater.* **2022**, *34*, 2204380.
[22] J. Zhang, X. Peng, H. Wu, G. Zhang, Y. Chen, W. Cai, Z. Pan, H. Rao, X. Zhong, *Angew. Chem., Int. Ed.* **2025**, *64*, 202423655.
[23] Z. Zhang, Y. Feng, J. Ding, Q. Ma, H. Zhang, J. Zhang, M. Li, T. Geng, W. Gao, Y. Wang, B. Zhang, T. Pauporté, J.-X. Tang, H. Chen, J. Chen, C. Chen, *Nat. Commun.* **2025**, *16*, 753.
[24] Y. Yang, H. Chen, C. Liu, J. Xu, C. Huang, C. D. Malliakas, H. Wan, A. S. R. Bati, Z. Wang, R. P. Reynolds, I. W. Gilley, S. Kitade, T. E. Wiggins, S. Zeiske, S. Suragtkhuu, M. Batmunkh, L. X. Chen, B. Chen, M. G. Kanatzidis, E. H. Sargent, *Science* **2024**, *386*, 898.
[25] S. Fu, N. Sun, H. Chen, C. Liu, X. Wang, Y. Li, A. Abudulimu, Y. Xu, S. Ramakrishnan, C. Li, Y. Yang, H. Wan, Z. Huang, Y. Xian, Y. Yin, T. Zhu, H. Chen, A. Rahimi, M. M. Saeed, Y. Zhang, Q. Yu, D. S. Ginger, R. J. Ellingson, B. Chen, Z. Song, M. G. Kanatzidis, E. H. Sargent, Y. Yan, *Nat. Nanotechnol.* **2025**, *20*, 772.
[26] M. Li, Y. Yang, Z. Kuang, C. Hao, S. Wang, F. Lu, Z. Liu, J. Liu, L. Zeng, Y. Cai, Y. Mao, J. Guo, H. Tian, G. Xing, Y. Cao, C. Ma, N. Wang, Q. Peng, L. Zhu, W. Huang, J. Wang, *Nature* **2024**, *630*, 631.
[27] L. Mu, S. Wang, H. Liu, W. Li, L. Zhu, H. Wang, H. Chen, *Adv. Funct. Mater.* **2025**, *35*, 2415353.
[28] X. Tang, T. Zhang, W. Chen, H. Chen, Z. Zhang, X. Chen, H. Gu, S. Kang, C. Han, T. Xu, J. Cao, J. Zheng, X. Ou, Y. Li, Y. Li, *Adv. Mater.* **2024**, *36*, 2400218.
[29] Q. Zhang, J. Duan, Q. Guo, J. Zhang, D. Zheng, F. Yi, X. Yang, Y. Duan, Q. Tang, *Angew. Chem., Int. Ed.* **2022**, *61*, 202116632.
[30] S. Wang, M. W. Urban, *Nat. Rev. Mater.* **2020**, *5*, 562.
[31] T. Xie, B. D. Vogt, *ACS Appl. Mater. Interfaces* **2020**, *12*, 49277.
[32] B. P. Finkenauer, Y. Gao, X. Wang, Y. Tian, Z. Wei, C. Zhu, D. J. Rokke, L. Jin, L. Meng, Y. Yang, L. Huang, K. Zhao, L. Dou, *Cell Rep. Phys. Sci.* **2021**, *2*, 100320.
[33] M. V. Khenkin, A. K. M, I. Visoly-Fisher, S. Kolusheva, Y. Galagan, F. Di Giacomo, O. Vukovic, B. R. Patil, G. Sherafatipour, V. Turkovic, H.-G. Rubahn, M. Madsen, A. V. Mazanik, E. A. Katz, *ACS Appl. Energy Mater.* **2018**, *1*, 799.
[34] M. Saliba, M. Stolterfoht, C. M. Wolff, D. Neher, A. Abate, *Joule* **2018**, *2*, 1019.
[35] X. Deng, X. Wen, C. F. J. Lau, T. Young, J. Yun, M. A. Green, S. Huang, A. W. Y. Ho-Baillie, *J. Mater. Chem. C* **2016**, *4*, 9060.
[36] D. Bryant, N. Aristidou, S. Pont, I. Sanchez-Molina, T. Chotchunangatchaval, S. Wheeler, J. R. Durrant, S. A. Haque, *Energy Environ. Sci.* **2016**, *9*, 1655.
[37] P. Tolueinia, H. Khassaf, A. Shirazi Amin, Z. M. Tobin, S. P. Alpay, S. L. Suib, *ACS Appl. Energy Mater.* **2020**, *3*, 8240.
[38] Q. Wang, B. Chen, Y. Liu, Y. Deng, Y. Bai, Q. Dong, J. Huang, *Energy Environ. Sci.* **2017**, *10*, 516.
[39] N. Ahn, K. Kwak, M. S. Jang, H. Yoon, B. Y. Lee, J.-K. Lee, P. V. Pikhitsa, J. Byun, M. Choi, *Nat. Commun.* **2016**, *7*, 13422.
[40] G. Divitini, S. Cacovich, F. Matteocci, L. Cinà, A. Di Carlo, C. Ducati, *Nat. Energy* **2016**, *1*, 15012.
[41] Y.-H. Seo, J. H. Kim, D.-H. Kim, H.-S. Chung, S.-I. Na, *Nano Energy* **2020**, *77*, 105164.
[42] Y. Yu, F. Zhang, H. Yu, *Sol. Energy* **2020**, *209*, 408.
[43] P. Teng, S. Reichert, W. Xu, S.-C. Yang, F. Fu, Y. Zou, C. Yin, C. Bao, M. Karlsson, X. Liu, J. Qin, T. Yu, W. Tress, Y. Yang, B. Sun, C. Deibel, F. Gao, *Matter* **2021**, *4*, 3710.
[44] J. Fan, Y. Ma, C. Zhang, C. Liu, W. Li, R. E. I. Schropp, Y. Mai, *Adv. Energy Mater.* **2018**, *8*, 1703421.
[45] J. Yang, W. Sheng, X. Li, Y. Zhong, Y. Su, L. Tan, Y. Chen, *Adv. Funct. Mater.* **2023**, *33*, 2214984.
[46] Z. Chen, Q. Cheng, H. Chen, Y. Wu, J. Ding, X. Wu, H. Yang, H. Liu, W. Chen, X. Tang, X. Lu, Y. Li, Y. Li, *Adv. Mater.* **2023**, *35*, 2300513.
[47] C. Ge, X. Liu, Z. Yang, H. Li, W. Niu, X. Liu, Q. Dong, *Angew. Chem., Int. Ed.* **2022**, *61*, 202116602.
[48] Y. Shen, T. Zhang, G. Xu, J. A. Steele, X. Chen, W. Chen, G. Zheng, J. Li, B. Guo, H. Yang, Y. Wu, X. Lin, T. Alshahrani, W. Yin, J. Zhu, F. Wang, A. Amassian, X. Gao, X. Zhang, F. Gao, Y. Li, Y. Li, *Nature* **2024**, *635*, 882.
[49] M. Khenkin, H. Köbler, M. Remec, R. Roy, U. Erdil, J. Li, N. Phung, G. Adwan, G. Paramasivam, Q. Emery, E. Unger, R. Schlatmann, C. Ulbrich, A. Abate, *Energy Environ. Sci.* **2024**, *17*, 602.

[50] F.-S. Zu, P. Amsalem, I. Salzmann, R.-B. Wang, M. Ralaiarisoa, S. Kowarik, S. Duhm, N. Koch, *Adv. Opt. Mater.* **2017**, *5*, 1700139.
[51] E. J. Juarez-Perez, L. K. Ono, M. Maeda, Y. Jiang, Z. Hawash, Y. Qi, *J. Mater. Chem. A* **2018**, *6*, 9604.
[52] Z. Song, C. Wang, A. B. Phillips, C. R. Grice, D. Zhao, Y. Yu, C. Chen, C. Li, X. Yin, R. J. Ellingson, M. J. Heben, Y. Yan, *Sustain. Energy Fuels* **2018**, *2*, 2460.
[53] X. Tang, M. Brandl, B. May, I. Levchuk, Y. Hou, M. Richter, H. Chen, S. Chen, S. Kahmann, A. Osvet, F. Maier, H.-P. Steinrück, R. Hock, G. J. Matt, C. J. Brabec, *J. Mater. Chem. A* **2016**, *4*, 15896.
[54] Y. Li, X. Xu, C. Wang, B. Ecker, J. Yang, J. Huang, Y. Gao, *J. Phys. Chem. C.* **2017**, *121*, 3904.
[55] S. Wang, Y. Jiang, E. J. Juarez-Perez, L. K. Ono, Y. Qi, *Nat. Energy* **2016**, *2*, 16195.
[56] Q. Chen, H. Zhou, T.-B. Song, S. Luo, Z. Hong, H.-S. Duan, L. Dou, Y. Liu, Y. Yang, *Nano Lett.* **2014**, *14*, 4158.
[57] F. Liu, Q. Dong, M. K. Wong, A. B. Djurišić, A. Ng, Z. Ren, Q. Shen, C. Surya, W. K. Chan, J. Wang, A. M. C. Ng, C. Liao, H. Li, K. Shih, C. Wei, H. Su, J. Dai, *Adv. Energy Mater.* **2016**, *6*, 1502206.
[58] P. H. Joshi, L. Zhang, I. M. Hossain, H. A. Abbas, R. Kottokkaran, S. P. Nehra, M. Dhaka, M. Noack, V. L. Dalal, *AIP Adv.* **2016**, *6*, 115114.
[59] L. Wu, S. Hu, F. Yang, G. Li, J. Wang, W. Zuo, J. J. Jerónimo-Rendon, S.-H. Turren-Cruz, M. Saba, M. Saliba, M. K. Nazeeruddin, J. Pascual, M. Li, A. Abate, *Nat. Rev. Mater.* **2025**, *10*, 536.
[60] C. C. Boyd, R. Cheacharoen, T. Leijtens, M. D. McGehee, *Chem. Rev.* **2019**, *119*, 3418.
[61] E. J. Juarez-Perez, L. K. Ono, Y. Qi, *J. Mater. Chem. A* **2019**, *7*, 16912.
[62] Z. Liu, P. Liu, M. Li, T. He, T. Liu, L. Yu, M. Yuan, *Adv. Energy Mater.* **2022**, *12*, 2200111.
[63] L. Ma, D. Guo, M. Li, C. Wang, Z. Zhou, X. Zhao, F. Zhang, Z. Ao, Z. Nie, *Chem. Mater.* **2019**, *31*, 8515.
[64] Z. Song, A. Abate, S. C. Watthage, G. K. Liyanage, A. B. Phillips, U. Steiner, M. Graetzel, M. J. Heben, *Adv. Energy Mater.* **2016**, *6*, 1600846.
[65] J. M. Frost, K. T. Butler, F. Brivio, C. H. Hendon, M. van Schilfgaarde, A. Walsh, *Nano Lett.* **2014**, *14*, 2584.
[66] A. M. A. Leguy, Y. Hu, M. Campoy-Quiles, M. I. Alonso, O. J. Weber, P. Azarhoosh, M. van Schilfgaarde, M. T. Weller, T. Bein, J. Nelson, P. Docampo, P. R. F. Barnes, *Chem. Mater.* **2015**, *27*, 3397.
[67] S. Yang, Y. Wang, P. Liu, Y.-B. Cheng, H. J. Zhao, H. G. Yang, *Nat. Energy* **2016**, *1*, 15016.
[68] J. Y. Ma, H. J. Yan, M. H. Li, J. K. Sun, Y. X. Chen, D. Wang, J. S. Hu, *Nanoscale* **2020**, *12*, 7759.
[69] J. Yang, B. D. Siempelkamp, D. Liu, T. L. Kelly, *ACS Nano* **2015**, *9*, 1955.
[70] J. Huang, S. Tan, P. D. Lund, H. Zhou, *Energy Environ. Sci.* **2017**, *10*, 2284.
[71] H. J. Snaith, A. Abate, J. M. Ball, G. E. Eperon, T. Leijtens, N. K. Noel, S. D. Stranks, J. T.-W. Wang, K. Wojciechowski, W. Zhang, *J. Phys. Chem. Lett.* **2014**, *5*, 1511.
[72] Z. Xiao, Y. Yuan, Y. Shao, Q. Wang, Q. Dong, C. Bi, P. Sharma, A. Gruverman, J. Huang, *Nat. Mater.* **2015**, *14*, 193.
[73] J. M. Azpiroz, E. Mosconi, J. Bisquert, F. De Angelis, *Energy Environ. Sci.* **2015**, *8*, 2118.
[74] N. Phung, A. Mattoni, J. A. Smith, D. Skroblin, H. Köbler, L. Choubrac, J. Breternitz, J. Li, T. Unold, S. Schorr, C. Gollwitzer, I. G. Scheblykin, E. L. Unger, M. Saliba, S. Meloni, A. Abate, A. Merdasa, *Joule* **2022**, *6*, 2152.
[75] J. Mizusaki, K. Arai, K. Fueki, *Solid State Ionics* **1983**, *11*, 203.
[76] E. L. Unger, E. T. Hoke, C. D. Bailie, W. H. Nguyen, A. R. Bowring, T. Heumüller, M. G. Christoforo, M. D. McGehee, *Energy Environ. Sci.* **2014**, *7*, 3690.
[77] D. H. Kang, N. G. Park, *Adv.Mater* **2019**, *31*, 1805214.
[78] D. He, D. Ma, R. Li, B. Liu, Q. Zhou, H. Yang, S. Lu, Z. Zhang, C. Li, X. Li, L. Ding, J. Feng, J. Yi, J. Chen, *ACS Energy Lett.* **2024**, *9*, 2615.
[79] W.-J. Yin, T. Shi, Y. Yan, *Adv. Mater.* **2014**, *26*, 4653.
[80] M. Abdi-Jalebi, Z. Andaji-Garmaroudi, S. Cacovich, C. Stavrakas, B. Philippe, J. M. Richter, M. Alsari, E. P. Booker, E. M. Hutter, A. J. Pearson, S. Lilliu, T. J. Savenije, H. Rensmo, G. Divitini, C. Ducati, R. H. Friend, S. D. Stranks, *Nature* **2018**, *555*, 497.
[81] D.-T. Nguyen, A. D. Bui, K. Huang, T. L. Leung, L.-C. Chang, K. Nguyen, G. D. Tabi, T. Trân-Phú, H. Nguyen, A. Ho-Baillie, P. Kluth, K. Weber, T. White, T. Duong, *Sol. RRL* **2024**, *8*, 2400113.
[82] I. M. Hermes, Y. Hou, V. W. Bergmann, C. J. Brabec, S. A. L. Weber, *J. Phys. Chem. Lett.* **2018**, *9*, 6249.
[83] C. Chen, Z. Song, C. Xiao, R. A. Awni, C. Yao, N. Shrestha, C. Li, S. S. Bista, Y. Zhang, L. Chen, R. J. Ellingson, C.-S. Jiang, M. Al-Jassim, G. Fang, Y. Yan, *ACS Energy Lett.* **2020**, *5*, 2560.
[84] P. Xu, J. Liu, S. Wang, J. Chen, B. Han, Y. Meng, S. Yang, L. Xie, M. Yang, R. Jia, Z. Ge, *Mater. Horiz.* **2023**, *10*, 5223.
[85] J. Yang, W. Sheng, X. Li, Y. Zhong, Y. Su, L. Tan, Y. Chen, *Adv. Funct. Mater.* **2023**, *33*, 2214984.
[86] Z. Chen, Q. Cheng, H. Chen, Y. Wu, J. Ding, X. Wu, H. Yang, H. Liu, W. Chen, X. Tang, X. Lu, Y. Li, Y. Li, *Adv. Mater.* **2023**, *35*, 2300513.
[87] X. Li, B. Ding, J. Huang, Z. Zhang, H. Dong, H. Yu, Z. Liu, L. Dai, Y. Shen, Y. Ding, P. J. Dyson, M. K. Nazeeruddin, M. Wang, *Adv. Mater.* **2024**, *37*, 2410338.
[88] T. Xue, B. Fan, K.-J. Jiang, Q. Guo, X. Hu, M. Su, E. Zhou, Y. Song, *Energy Environ. Sci.* **2024**, *17*, 2621.
[89] Y. Tang, Z. Zhang, G. Li, C. Qin, Z. Su, H. Liu, F. Yang, Y. Yang, M. H. Aldamasy, L. Deng, L. Wang, A. Abate, Y. Liu, M. Li, *Adv. Mater.* **2025**, *37*, 2420378.
[90] X. Sun, W. Shi, T. Liu, J. Cheng, X. Wang, P. Xu, W. Zhang, X. Zhao, W. Guo, *Science* **2025**, *388*, 957.
[91] H. Wang, S. Su, Y. Chen, M. Ren, S. Wang, Y. Wang, C. Zhu, Y. Miao, C. Ouyang, Y. Zhao, *Nature* **2024**, *634*, 1091.
[92] X. Qian, Y. Shen, L.-J. Zhang, M. Guo, X.-Y. Cai, Y. Lu, H. Liu, Y.-F. Zhang, Y. Tang, L. Chen, Y. Tang, J. Wang, W. Zhou, X. Gao, H. Mao, Y. Li, J.-X. Tang, S.-T. Lee, *ACS Nano* **2022**, *16*, 17973.
[93] X. Meng, Z. Cai, Y. Zhang, X. Hu, Z. Xing, Z. Huang, Z. Huang, Y. Cui, T. Hu, M. Su, X. Liao, L. Zhang, F. Wang, Y. Song, Y. Chen, *Nat. Commun.* **2020**, *11*, 3016.
[94] D. R. Ceratti, A. V. Cohen, R. Tenne, Y. Rakita, L. Snarski, N. P. Jasti, L. Cremonesi, R. Cohen, M. Weitman, I. Rosenhek-Goldian, I. Kaplan-Ashiri, T. Bendikov, V. Kalchenko, M. Elbaum, M. A. C. Potenza, L. Kronik, G. Hodes, D. Cahen, *Mater. Horiz.* **2021**, *8*, 1570.
[95] S. Shao, M. Abdu-Aguye, L. Qiu, L.-H. Lai, J. Liu, S. Adjokatse, F. Jahani, M. E. Kamminga, G. H. ten Brink, T. T. M. Palstra, B. J. Kooi, J. C. Hummelen, M. Antonietta Loi, *Energy Environ. Sci.* **2016**, *9*, 2444.
[96] C. Zhao, B. Chen, X. Qiao, L. Luan, K. Lu, B. Hu, *Adv. Energy Mater.* **2015**, *5*, 201570076.
[97] F. C. Liang, F. C. Jhuang, Y. H. Fang, J. S. Benas, W. C. Chen, Z. L. Yan, W. C. Lin, C. J. Su, Y. Sato, T. Chiba, J. Kido, C. C. Kuo, *Adv.Mater* **2023**, *35*, 2207617.
[98] M. Lu, Y. Zhang, S. Wang, J. Guo, W. W. Yu, A. L. Rogach, *Adv. Funct. Mater.* **2019**, *29*, 1902008.
[99] X. Li, Y. Wu, S. Zhang, B. Cai, Y. Gu, J. Song, H. Zeng, *Adv. Funct. Mater.* **2016**, *26*, 2435.
[100] X. Zhang, H. Liu, W. Wang, J. Zhang, B. Xu, K. L. Karen, Y. Zheng, S. Liu, S. Chen, K. Wang, X. W. Sun, *Adv. Mater.* **2017**, *29*, 1606405.
[101] L. Protesescu, S. Yakunin, M. I. Bodnarchuk, F. Bertolotti, N. Masciocchi, A. Guagliardi, M. V. Kovalenko, *J. Am. Chem. Soc.* **2016**, *138*, 14202.
[102] G. Li, Z. Su, L. Canil, D. Hughes, M. H. Aldamasy, J. Dagar, S. Trofimov, L. Wang, W. Zuo, J. J. Jerónimo-Rendon, M. M. Byranvand, C. Wang, R. Zhu, Z. Zhang, F. Yang, G. Nasti, B. Naydenov, W. C.

Tsoi, Z. Li, X. Gao, Z. Wang, Y. Jia, E. Unger, M. Saliba, M. Li, A. Abate, *Science* **2023**, *379*, 399.
[103] Q. Zhang, C.-Y. Shi, D.-H. Qu, Y.-T. Long, B. L. Feringa, H. Tian, *Sci.Adv* **2018**, *4*, aat8192.
[104] X. Li, B. Ding, J. Huang, Z. Zhang, H. Dong, H. Yu, Z. Liu, L. Dai, Y. Shen, Y. Ding, P. J. Dyson, M. K. Nazeeruddin, M. Wang, *Adv. Mater.* **2025**, *37*, 2410338.
[105] Y. Tang, Z. Zhang, G. Li, C. Qin, Z. Su, H. Liu, F. Yang, Y. Yang, M. H. Aldamasy, L. Deng, L. Wang, A. Abate, Y. Liu, M. Li, *Adv.Mater* **2025**, *37*, 2420378.
[106] X. Qian, Y. Shen, L. J. Zhang, M. Guo, X. Y. Cai, Y. Lu, H. Liu, Y. F. Zhang, Y. Tang, L. Chen, Y. Tang, J. Wang, W. Zhou, X. Gao, H. Mao, Y. Li, J. X. Tang, S. T. Lee, *ACS Nano* **2022**, *16*, 17973.
[107] X. Meng, Z. Cai, Y. Zhang, X. Hu, Z. Xing, Z. Huang, Z. Huang, Y. Cui, T. Hu, M. Su, X. Liao, L. Zhang, F. Wang, Y. Song, Y. Chen, *Nat. Commun.* **2020**, *11*, 3016.
[108] Z. Chen, G. Brocks, S. Tao, P. A. Bobbert, *Nat. Commun.* **2021**, *12*, 2687.
[109] Z. Zhang, W. Chen, X. Jiang, J. Cao, H. Yang, H. Chen, F. Yang, Y. Shen, H. Yang, Q. Cheng, X. Chen, X. Tang, S. Kang, X.-m. Ou, C. J. Brabec, Y. Li, Y. Li, *Nat. Energy* **2024**, *9*, 592.
[110] J. Tian, C. Liu, K. Forberich, A. Barabash, Z. Xie, S. Qiu, J. Byun, Z. Peng, K. Zhang, T. Du, S. Sathasivam, T. J. Macdonald, L. Dong, C. Li, J. Zhang, M. Halik, V. M. Le Corre, A. Osvet, T. Heumüller, N. Li, Y. Zhou, L. Lüer, C. J. Brabec, *Nat. Commun.* **2025**, *16*, 154.
[111] S. Kim, D. Im, Y. Yun, D. Vidyasagar, S. W. Yang, W. C. Choi, R. K. Gunasekaran, S. Lee, Y. T. Kim, M. Y. Woo, D. H. Kim, J. H. Noh, J. Heo, R. B. K. Chung, S. Lee, *Adv. Energy Mater.* **2025**, *15*, 2404366.
[112] L. Kuai, Y. Wang, Z. Zhang, Y. Yang, Y. Qin, T. Wu, Y. Li, Y. Li, T. Song, X. Gao, L. Wang, B. Sun, *Sol. RRL* **2019**, *3*, 1900053.
[113] R. Lin, K. Xiao, Z. Qin, Q. Han, C. Zhang, M. Wei, M. I. Saidaminov, Y. Gao, J. Xu, M. Xiao, A. Li, J. Zhu, E. H. Sargent, H. Tan, *Nat. Energy* **2019**, *4*, 864.
[114] D. Yu, M. Pan, G. Liu, X. Jiang, X. Wen, W. Li, S. Chen, W. Zhou, H. Wang, Y. Lu, M. Ma, Z. Zang, P. Cheng, Q. Ji, F. Zheng, Z. Ning, *Nat. Energy* **2024**, *9*, 298.
[115] M. Yang, Y. Bai, Y. Meng, R. Tian, K. Sun, X. Lu, H. Pan, J. Wang, S. Zhou, J. Zhang, Z. Song, Y. Wang, C. Liu, Z. Ge, *Adv. Mater.* **2025**, *37*, 2415627.
[116] D. Wang, M. Chen, X. Lei, Y. Wang, Y. Bao, X. Huang, P. Zhu, J. Zeng, X. Wang, S. Tsang, F. Li, B. Xu, A. K. Y. Jen, *Adv. Mater.* **2024**, *36*, 2411677.
[117] P. Luo, X.-Y. Sun, Y. Li, L. Yang, W.-Z. Shao, L. Zhen, C.-Y. Xu, *ACS Appl. Energy Mater.* **2021**, *4*, 13504.
[118] S. Yang, Z. Xu, S. Xue, P. Kandlakunta, L. Cao, J. Huang, *Adv. Mater.* **2019**, *31*, 1805547.
[119] A. G. Boldyreva, L. A. Frolova, I. S. Zhidkov, L. G. Gutsev, E. Z. Kurmaev, B. R. Ramachandran, V. G. Petrov, K. J. Stevenson, S. M. Aldoshin, P. A. Troshin, *J. Phys. Chem. Lett.* **2020**, *11*, 2630.
[120] B. K. Durant, H. Afshari, S. Singh, B. Rout, G. E. Eperon, I. R. Sellers, *ACS Energy Lett.* **2021**, *6*, 2362.
[121] A. R. Kirmani, T. A. Byers, Z. Ni, K. VanSant, D. K. Saini, R. Scheidt, X. Zheng, T. B. Kum, I. R. Sellers, L. McMillon-Brown, J. Huang, B. Rout, J. M. Luther, *Nat. Commun.* **2024**, *15*, 696.

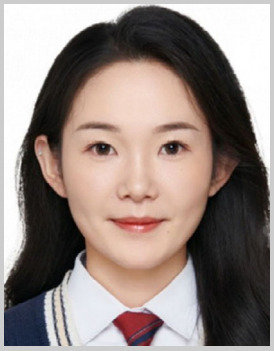

Xiaochun Zhang is currently a Research Assistant at Southeast University. She received her Bachelor's degree from Chifeng University in 2022 and her Master's degree from Liaoning Normal University in 2025. Her research focuses on high-performance perovskite solar cells.

Qing Cao is a Provost's Postdoctoral Society of Science Fellow at the University of Notre Dame. She received her Ph.D. in Chemistry from the Free University of Berlin, Germany, in 2024. Her research focuses on nanomaterials and their applications in energy conversion and storage. She is particularly interested in exploring the structure-property relationships of two-dimensional materials and developing advanced nano-bio interfaces for sustainable and multifunctional energy devices.

Luyao Wang is currently an associate professor at the College of Chemistry and Chemical Engineering, Xiamen University. He received his PhD from Shanghai Jiao Tong University in 2024 and pursued post-doctoral research at The Hong Kong Polytechnic University from 2024 to 2025. His research interests include the design and application of novel optoelectronic materials, novel perovskite solar cells, and artificial intelligence.

Tiankai Zhang received his B.S. in Physics from Nanjing University and PhD from the School of Electrical Engineering at the Chinese University of Hong Kong. He is now a Professor in the School of Materials Science and Engineering at the Southeast University. His research interests include the design and optimization of hybrid perovskite and organic semiconductors for applications in optoelectronic devices.

Kaiyu Fu is an Assistant Professor of Chemistry at the University of Notre Dame. He received his Ph.D. in Chemistry from the University of Notre Dame in 2018 and completed postdoctoral research at Stanford University. Dr. Fu's research integrates electrochemistry, nanoscience, and synthetic biology to advance analytical technologies and biomedical applications. His current work focuses on nanoscale electrochemical processes, point-of-care electrochemical biosensing, and nanobiotechnology for precise molecular recognition and disease diagnostics.

Zhe Li is Reader in Materials Science at the School of Engineering and Materials Science, Queen Mary University of London. He received his Ph.D. from Cavendish Laboratory at University of Cambridge in 2012 and worked as a research associate/research fellow/junior group leader at Imperial College London (2012–2015) and Swansea University (2015–2017), and as a lecturer of Energy Materials at School of Engineering, Cardiff University (2018–2019). His main research interest includes organic, perovskite, and quantum dot photovoltaic cells, including in emerging target applications, stability analysis, and advanced materials and device characterisation.

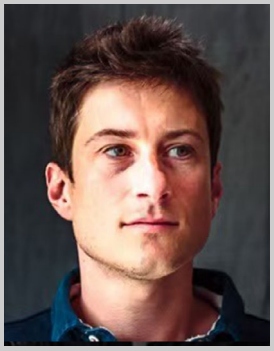

Antonio Abate is a team leader at the Helmholtz-Zentrum Berlin and a tenure-track professor at the University of Naples Federico II. His research focuses on solar energy conversion using perovskite solar cells and advanced photovoltaic materials, employing supramolecular chemistry to enhance device performance and stability. A Highly Cited Researcher since 2018, he previously led solar cell research at the University of Fribourg and held postdoctoral positions at EPFL, Oxford, and Cambridge. He received his Ph.D. from Politecnico di Milano in 2011.

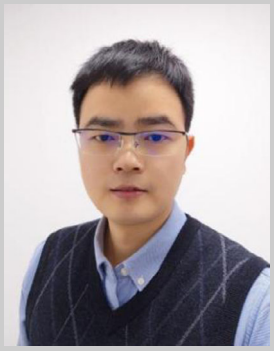

Meng Li is a professor at the School of Nanoscience and Materials Engineering, Henan University. His work focuses on organic-inorganic hybrid semiconductors for optoelectronic devices, especially perovskite solar cells and quantum dot LEDs (QLEDs). His research covers materials design, interface engineering, thin-film processing, and device physics, aiming to improve performance, stability, and scalability. He earned his Ph.D. from Soochow University and conducted postdoctoral research at the Helmholtz-Zentrum Berlin (HZB) in Germany, focusing on the stability of perovskite thin films in cyclic environments. His interests include lead-based and lead-free perovskite devices, self-assembled monolayers, and perovskite crystal dynamics.

Guixiang Li is a Professor at the School of Materials Science and Engineering, Southeast University. He received his Ph.D. from the Helmholtz-Zentrum Berlin (HZB), Germany, and conducted postdoctoral research at the École Polytechnique Fédérale de Lausanne (EPFL), Switzerland, and Northwestern University, USA. His research focuses on the design, processing, and integration of highly stable perovskite optoelectronic devices. He is particularly interested in understanding the degradation mechanisms of perovskite photovoltaics and developing stress-resilient device architectures. His group aims to bridge fundamental materials chemistry with scalable fabrication and integration strategies, advancing the practical deployment of next-generation optoelectronic devices.